

Data-Driven Reduced-Order Models for Port-Hamiltonian Systems with Operator Inference

Yuwei Geng^a, Lili Ju^a, Boris Kramer^b, Zhu Wang^{a,*}

^a*Department of Mathematics, University of South Carolina, Columbia, SC 29208, USA*

^b*Department of Mechanical and Aerospace Engineering, University of California San Diego, La Jolla, CA 92093, USA*

Abstract

Hamiltonian operator inference has been developed in [Sharma, H., Wang, Z., Kramer, B., *Physica D: Non-linear Phenomena*, 431, p.133122, 2022] to learn structure-preserving reduced-order models (ROMs) for Hamiltonian systems. The method constructs a low-dimensional model using only data and knowledge of the functional form of the Hamiltonian. The resulting ROMs preserve the intrinsic structure of the system, ensuring that the mechanical and physical properties of the system are maintained. In this work, we extend this approach to port-Hamiltonian systems, which generalize Hamiltonian systems by including energy dissipation, external input, and output. Based on snapshots of the system's state and output, together with the information about the functional form of the Hamiltonian, reduced operators are inferred through optimization and are then used to construct data-driven ROMs. To further alleviate the complexity of evaluating nonlinear terms in the ROMs, a hyper-reduction method via discrete empirical interpolation is applied. Accordingly, we derive error estimates for the ROM approximations of the state and output. Finally, we demonstrate the structure preservation, as well as the accuracy of the proposed port-Hamiltonian operator inference framework, through numerical experiments on a linear mass-spring-damper problem and a nonlinear Toda lattice problem.

Keywords: port-Hamiltonian system, operator inference, model order reduction, data-driven modeling

1. Introduction

A port-Hamiltonian (pH) system [1] provides a mathematical framework for modeling and controlling a wide range of physical systems, with applications in fields such as electrical circuits, thermodynamics, chemical processes, and mechanical engineering [2]. Unlike a traditional Hamiltonian system, which describes the evolution of a physical system in time based on energy conservation, a pH system incorporates energy dissipation and external inputs and outputs through *ports*. We consider a finite-dimensional pH system of the form

$$\begin{cases} \dot{\mathbf{x}}(t) = (\mathbf{J} - \mathbf{R})\nabla_{\mathbf{x}}H(\mathbf{x}(t)) + \mathbf{B}\mathbf{u}(t), & (1a) \\ \mathbf{y}(t) = \mathbf{B}^T\nabla_{\mathbf{x}}H(\mathbf{x}(t)), & (1b) \end{cases}$$

*Corresponding author

Email addresses: ygeng@email.sc.edu (Yuwei Geng), ju@math.sc.edu (Lili Ju), bmramer@ucsd.edu (Boris Kramer), wangzhu@math.sc.edu (Zhu Wang)

with $\mathbf{x}(0) = \mathbf{x}^0$, where $\mathbf{x}(t) \in \mathbb{R}^n$ represents the n -dimensional state vector, $H(\mathbf{x})$ is the Hamiltonian function, which is continuously differentiable and represents the internal energy of the system, the matrix $\mathbf{J} = -\mathbf{J}^\top \in \mathbb{R}^{n \times n}$ is skew-symmetric, describing the interconnection of the system's energy storage elements; the matrix $\mathbf{R} = \mathbf{R}^\top \in \mathbb{R}^{n \times n}$ is symmetric and positive semi-definite, characterizing the energy dissipation in the system, $\mathbf{B} \in \mathbb{R}^{n \times m}$ is the port matrix, which describes the modalities through which energy is imported into or exported from the system, $\mathbf{u}(t) \in \mathbb{R}^m$ represents the external input vector, and $\mathbf{y}(t) \in \mathbb{R}^m$ is the system's output vector. Based on the structural properties of \mathbf{J} and \mathbf{R} , one can conclude that the Hamiltonian function satisfies the dissipation inequality: for any $t^2 > t^1 \geq 0$,

$$\begin{aligned} H(\mathbf{x}(t^2)) - H(\mathbf{x}(t^1)) &= \int_{t^1}^{t^2} (\nabla_{\mathbf{x}} H(\mathbf{x}(t)))^\top [(\mathbf{J} - \mathbf{R})\nabla_{\mathbf{x}} H(\mathbf{x}(t)) + \mathbf{B}\mathbf{u}(t)] dt \\ &\leq \int_{t^1}^{t^2} \mathbf{y}(t)^\top \mathbf{u}(t) dt. \end{aligned} \quad (2)$$

Given an initial condition, the high-dimensional dynamical system (1) can be simulated using geometric numerical integration schemes [3]. However, when the system needs to be solved repeatedly, those high-dimensional numerical simulations become computationally expensive. Model order reduction (MOR) can be used to design a surrogate model with fewer degrees of freedom to accelerate the simulations. It has been successfully applied to many engineering problems, particularly those governed by differential equations. Various techniques have been developed, including the reduced basis (RB) method [4], proper orthogonal decomposition (POD) [5], dynamic mode decomposition (DMD) [6, 7], operator inference [8, 9], and interpolatory model reduction [10, 11], among others. A common idea of these techniques is to extract characteristic features from either training data or the model equations and build a ROM during an offline stage, which can then be used for simulations at a low cost during an online stage. For an overview of projection-based MOR for parametric dynamical systems, we refer the reader to [12, 13].

For systems with certain structure, such as Lagrangian, Hamiltonian and pH systems, failure to satisfy the structure at the ROM level can result in unphysical solutions and unstable behavior [14, 15]. For instance, the reduced-order operators for \mathbf{J} and \mathbf{R} in (1) may lose their respective skew-symmetry or symmetric semi-positive definiteness properties. To address this issue, structure-preserving MOR techniques have been introduced. Similar to other types of MOR, structure-preserving ROMs can be constructed either intrusively or non-intrusively. Intrusive methods include the POD-based Galerkin projection method for Hamiltonian systems [16, 17, 18], POD/ \mathcal{H}_2 -based Petrov-Galerkin projection method for pH systems [19, 20], proper symplectic decomposition (PSD) [21], a variationally consistent approach for canonical Hamiltonian systems [22], and RB-ROMs for Hamiltonian systems [23, 24, 25, 26]. Additionally, to efficiently evaluate nonlinear terms in ROMs, the discrete empirical interpolation method (DEIM), originally developed in [27, 28] for interpolating the nonlinear terms over selected sparse sample points, has been extended in [29] to the structure-preserving setting for Hamiltonian ROMs. Unlike classical model reduction approaches that use linear subspaces, the authors in [30, 31, 32] combine quadratic or nonlinear manifold learning with symplectic auto-encoders to construct an intrusive ROM for Hamiltonian systems. Non-intrusive structure-preserving MOR techniques, on the other hand, construct ROMs by using only snapshot data and some prior knowledge of the dynamical system. Hence, they are sometimes referred to as 'glass box' approaches. Recent work includes learning of canonical Hamiltonian ROMs based on operator inference, where the linear part of the Hamiltonian gradient is inferred through constrained least-squares solutions [33]. Non-canonical Hamiltonian operator inference ROMs have been developed in [34], assuming the entire Hamiltonian function is known and inferring the reduced operator associated with the linear differential operator. Gradient-preserving operator inference (GP-OpInf) has been developed for conservative

or dissipative systems in [35]. A tensor-based operator inference approach has been introduced in [36] to construct a ROM with the Hamiltonian structure while capturing parametric dependencies.

To date, data-driven model reduction for *nonlinear* pH systems remains an open problem. On the other hand, for linear pH systems, there have been some works. In [37], the Loewner framework is applied to derive a state-space model using only input-output time-domain data, and the pH system is then inferred by solving an associated optimization problem. In [38], the pH dynamic mode decomposition method is developed to infer linear pH ROMs, in which the reduced-order operators for \mathbf{J} and \mathbf{R} are found in an iterative way under the assumption that the quadratic Hamiltonian is known.

In this paper, we propose a pH operator inference (pH-OpInf) method to construct ROMs for linear and nonlinear pH systems, *using snapshot data of the state, external input, and output, along with knowledge of the functional form of the Hamiltonian*. The main contributions of our work include:

- (i) We propose two optimization formulations to learn the structure-preserving reduced-order operators for constructing ROMs of pH systems. In particular, the optimization in the first formulation is decoupled into two subtasks in the second formulation to facilitate its solution.
- (ii) We incorporate hyper-reduction into the structure-preserving ROMs for nonlinear pH systems.
- (iii) We derive *a priori* error estimates for the reduced-order approximations of the inferred structure-preserving ROM for both state and output variables.

The remainder of this paper is organized as follows. In Section 2, we review a Galerkin projection-based ROM as the state-of-the-art intrusive MOR method for reducing the pH system (1), and employ DEIM to ensure efficient simulation of the nonlinear ROM. Section 3 proposes the new pH-OpInf method and suggests two optimization problems to find the reduced-order operators. In Section 4, we analyze the resulting structure-preserving ROMs and derive *a priori* error estimates for both state and output approximations. The effectiveness of the proposed ROMs is numerically demonstrated through two examples in Section 5. Finally, some concluding remarks are drawn in Section 6.

2. Background on Projection-Based Reduced-Order Models for the Port-Hamiltonian System

The POD method [39] has been widely used in MOR to find a set of reduced basis vectors from snapshot data, which are then used to construct the ROM evolution equations. In practice, the basis vectors are often computed using singular value decomposition (SVD) on the array of snapshots, and the associated left singular vectors are truncated to form the reduced basis. The truncation error provides empirical guidance on choosing the number of reduced basis vectors. By approximating the state variables in the subspace spanned by the reduced basis and projecting the original system onto either the same subspace or another low-dimensional space, one can construct a Galerkin or Petrov-Galerkin projection-based ROM. This workflow is intrusive, as it requires access to the matrices and vectors of the full-order model (FOM) to build the ROM. When applied to Hamiltonian or pH systems, such ROMs may alter the structural properties of the FOM and result in inaccurate and unphysical solutions. This limitation motivates the development of structure-preserving ROMs, see examples in [40, 20, 16]. In the following, we focus on Galerkin projection and the design of a structure-preserving ROM for the pH system (1).

2.1. Intrusive Structure-Preserving ROMs

Assume that the snapshot data for the state variables of the pH system (1) is given in matrix form as

$$\mathbf{X} := [\mathbf{x}(t^0), \mathbf{x}(t^1), \dots, \mathbf{x}(t^s)] \in \mathbb{R}^{n \times (s+1)}, \quad (3)$$

where $\mathbf{x}(t^i)$ is the state vector at the discrete time instances t^i , for $i = 0, 1, \dots, s$. For simplicity, we assume the snapshots are uniformly distributed, that is, $t^i = i\Delta t$ with a constant Δt that could be the time step size used in full-order simulations or a checkpoint at which solutions are stored. The POD basis matrix is denoted as $\Phi := [\phi_1, \phi_2, \dots, \phi_r]$, where ϕ_i is the i th left singular vector of \mathbf{X} associated with the singular value σ_i , and r is the dimension of the POD basis that is less than the rank d of \mathbf{X} . The dimension r is typically selected to ensure that the POD basis captures a significant portion of the snapshot energy. In particular, given a prescribed tolerance τ , r is chosen such that $\frac{\sum_{i=1}^r \sigma_i^2}{\sum_{i=1}^d \sigma_i^2} \geq \tau$. Note that $\Phi^\top \Phi = \mathbf{I}_r$. The reduced approximation employs the ansatz $\hat{\mathbf{x}}(t) = \Phi \mathbf{x}_r(t)$, where $\mathbf{x}_r(t) \in \mathbb{R}^r$ is the unknown POD coefficient vector.

Replacing $\mathbf{x}(t)$ with the reduced approximation $\hat{\mathbf{x}}(t)$, and applying Galerkin projection to (1), we obtain a low-dimensional ROM for the pH system (1), denoted as G-ROM:

$$\begin{cases} \dot{\mathbf{x}}_r(t) = \Phi^\top (\mathbf{J} - \mathbf{R}) \nabla_{\mathbf{x}} H(\Phi \mathbf{x}_r(t)) + \Phi^\top \mathbf{B} \mathbf{u}(t), \\ \mathbf{y}_r(t) = \mathbf{B}^\top \nabla_{\mathbf{x}} H(\Phi \mathbf{x}_r(t)), \end{cases} \quad (4a)$$

$$\quad (4b)$$

where $\mathbf{y}_r(t) \in \mathbb{R}^m$ is the reduced-order approximation of the output. Let us define the reduced Hamiltonian $H_r(\mathbf{x}_r(t)) := H(\Phi \mathbf{x}_r(t))$, then the rate of change of the reduced Hamiltonian during the ROM simulation is

$$\begin{aligned} \frac{d}{dt} H_r(\mathbf{x}_r(t)) &= [\nabla_{\mathbf{x}_r} H(\Phi \mathbf{x}_r(t))]^\top \frac{d\mathbf{x}_r(t)}{dt} \\ &= [\Phi^\top \nabla_{\mathbf{x}} H(\Phi \mathbf{x}_r(t))]^\top [\Phi^\top (\mathbf{J} - \mathbf{R}) \nabla_{\mathbf{x}} H(\Phi \mathbf{x}_r(t)) + \Phi^\top \mathbf{B} \mathbf{u}(t)] \\ &= [\nabla_{\mathbf{x}} H(\Phi \mathbf{x}_r(t))]^\top \Phi \Phi^\top \mathbf{J} \nabla_{\mathbf{x}} H(\Phi \mathbf{x}_r(t)) - [\nabla_{\mathbf{x}} H(\Phi \mathbf{x}_r(t))]^\top \Phi \Phi^\top \mathbf{R} \nabla_{\mathbf{x}} H(\Phi \mathbf{x}_r(t)) \\ &\quad + [\nabla_{\mathbf{x}} H(\Phi \mathbf{x}_r(t))]^\top \Phi \Phi^\top \mathbf{B} \mathbf{u}(t). \end{aligned}$$

Since the matrices $\Phi \Phi^\top \mathbf{J}$ and $\Phi \Phi^\top \mathbf{R}$ do not retain the same structural properties as \mathbf{J} and \mathbf{R} , integrating the equation from t^1 to t^2 shows that $H_r(\mathbf{x}_r(t^2)) - H_r(\mathbf{x}_r(t^1))$ is not guaranteed to remain bounded above by the integration of $\mathbf{y}_r(t)^\top \mathbf{u}(t)$ over $[t^1, t^2]$, as indicated by the dissipation inequality (2) for the FOM. Typically, the G-ROM is not ensured to be dissipative even when $\mathbf{u} \equiv \mathbf{0}$.

To overcome the same issue in MOR for a Hamiltonian system, the PSD method has been introduced in [21], which is specifically designed for systems with symplectic structures. Since the pH system (1) is more general, we adopt the method suggested in [16] and seek $\tilde{\mathbf{J}}_r$ and $\tilde{\mathbf{R}}_r$ such that

$$\Phi^\top \mathbf{J} = \tilde{\mathbf{J}}_r \Phi^\top \quad \text{and} \quad \Phi^\top \mathbf{R} = \tilde{\mathbf{R}}_r \Phi^\top.$$

Following a least-squares approximation, one identifies the reduced-order operators as

$$\tilde{\mathbf{J}}_r = \Phi^\top \mathbf{J} \Phi \quad \text{and} \quad \tilde{\mathbf{R}}_r = \Phi^\top \mathbf{R} \Phi.$$

Replacing $\Phi^\top \mathbf{J}$ and $\Phi^\top \mathbf{R}$ in (4) with $\tilde{\mathbf{J}}_r \Phi^\top$ and $\tilde{\mathbf{R}}_r \Phi^\top$, respectively, defining $\tilde{\mathbf{B}}_r = \Phi^\top \mathbf{B}$, and noticing that

$$\nabla_{\mathbf{x}_r} H_r(\mathbf{x}_r(t)) = \Phi^\top \nabla_{\mathbf{x}} H(\Phi \mathbf{x}_r(t)), \quad (5)$$

we obtain a structure-preserving Galerkin projection-based ROM (SP-G-ROM) for the pH system (1) as

$$\begin{cases} \dot{\mathbf{x}}_r(t) = (\tilde{\mathbf{J}}_r - \tilde{\mathbf{R}}_r) \nabla_{\mathbf{x}_r} H_r(\mathbf{x}_r(t)) + \tilde{\mathbf{B}}_r \mathbf{u}(t), \\ \mathbf{y}_r(t) = \tilde{\mathbf{B}}_r^\top \nabla_{\mathbf{x}_r} H_r(\mathbf{x}_r(t)) \end{cases} \quad (6a)$$

$$\quad (6b)$$

with the initial condition

$$\mathbf{x}_r(0) = \mathbf{\Phi}^\top \mathbf{x}^0. \quad (7)$$

Due to the same structure as its full-order counterpart, the time derivative of the reduced Hamiltonian is

$$\begin{aligned} \frac{d}{dt} H_r(\mathbf{x}_r(t)) &= [\nabla_{\mathbf{x}_r} H_r(\mathbf{x}_r(t))]^\top \frac{d\mathbf{x}_r(t)}{dt} \\ &= [\nabla_{\mathbf{x}_r} H_r(\mathbf{x}_r(t))]^\top \left[(\tilde{\mathbf{J}}_r - \tilde{\mathbf{R}}_r) \nabla_{\mathbf{x}_r} H_r(\mathbf{x}_r(t)) + \tilde{\mathbf{B}}_r \mathbf{u}(t) \right] \\ &\leq [\nabla_{\mathbf{x}_r} H_r(\mathbf{x}_r(t))]^\top \tilde{\mathbf{B}}_r \mathbf{u}(t) \quad (\text{as } \tilde{\mathbf{J}}_r = -\tilde{\mathbf{J}}_r^\top, \tilde{\mathbf{R}}_r = \tilde{\mathbf{R}}_r^\top \text{ and } \tilde{\mathbf{R}}_r \succcurlyeq \mathbf{0}) \\ &= \mathbf{y}_r(t)^\top \mathbf{u}(t). \end{aligned}$$

Thus, integrating the equation from t^1 to t^2 yields that $H_r(\mathbf{x}_r(t^2)) - H_r(\mathbf{x}_r(t^1))$ is bounded by $\int_{t^1}^{t^2} \mathbf{y}_r(t)^\top \mathbf{u}(t) dt$ from above, therefore, the dissipation inequality (2) holds at the reduced-order level.

Since the dimension r of the ROM is typically much smaller than n , simulating the SP-G-ROM is generally more computationally efficient than simulating the FOM. However, when $\nabla_{\mathbf{x}_r} H_r(\mathbf{x}_r(t))$ is nonlinear, the overall computational complexity still depends on n . Therefore, an additional approximation, termed hyper-reduction, is needed to accelerate the ROM simulation.

2.2. Hyper-Reduction of Nonlinear Hamiltonian ROMs

The nonlinear Hamiltonian function can be recast as

$$H(\mathbf{x}(t)) = \frac{1}{2} \mathbf{x}(t)^\top \mathbf{Q} \mathbf{x}(t) + N(\mathbf{x}(t)),$$

where $\mathbf{Q} \in \mathbb{R}^{n \times n}$ represents the quadratic part and $N(\mathbf{x})$ captures the remaining non-quadratic terms. After defining $\mathbf{Q}_r = \mathbf{\Phi}^\top \mathbf{Q} \mathbf{\Phi}$ and $N_r(\mathbf{x}_r(t)) = N(\mathbf{\Phi} \mathbf{x}_r(t))$, we have the gradient of the reduced Hamiltonian approximation as

$$\nabla_{\mathbf{x}_r} H_r(\mathbf{x}_r(t)) = \mathbf{Q}_r \mathbf{x}_r(t) + \nabla_{\mathbf{x}_r} N_r(\mathbf{x}_r(t)).$$

The calculation of $\nabla_{\mathbf{x}_r} N_r(\mathbf{x}_r(t))$ is expensive for large n . To reduce the computational cost, we apply the approach developed in [29], outlined below, that extends DEIM to such a nonlinear Hamiltonian function. Note that both standard DEIM [28, 41] and Q-DEIM [41] can be used to select interpolation points. We choose the latter because of its enhanced stability and accuracy. Since Q-DEIM is a variant of DEIM, we will continue to use ‘DEIM’ to refer to the hyper-reduction approach and label the associated hyper-reduced ROMs.

First, without loss of generality, $N_r(\mathbf{x}_r(t))$ can be written as

$$N_r(\mathbf{x}_r(t)) = \sum_{i=1}^d c_i h_i(\mathbf{\Phi} \mathbf{x}_r(t)) = \mathbf{c}^\top \mathbf{h}(\mathbf{\Phi} \mathbf{x}_r(t)),$$

where $d \in \mathbb{N}$, $\mathbf{c} \in \mathbb{R}^d$ is a constant vector and $\mathbf{h}(\cdot)$ is a vector-valued function. Correspondingly, its gradient is

$$\nabla_{\mathbf{x}_r} N_r(\mathbf{x}_r(t)) = \mathbf{\Phi}^\top J_h^\top(\mathbf{\Phi} \mathbf{x}_r(t)) \mathbf{c},$$

in which $J_h(\cdot) \in \mathbb{R}^{d \times n}$ is the Jacobian of $\mathbf{h}(\cdot)$. Second, the approach requires forming the nonlinear snapshot matrix

$$M_J = [J_h(\mathbf{\Phi} \mathbf{\Phi}^\top \mathbf{x}(t^0)) \mathbf{\Phi}, \dots, J_h(\mathbf{\Phi} \mathbf{\Phi}^\top \mathbf{x}(t^s)) \mathbf{\Phi}] \in \mathbb{R}^{d \times r(s+1)},$$

which is used to determine the nonlinear basis $\Psi \in \mathbb{R}^{d \times m}$ and the interpolation matrix $\mathbf{P} := [\mathbf{e}_{\varphi_1}, \dots, \mathbf{e}_{\varphi_m}]$ using DEIM, where \mathbf{e}_i is the i th unit vector of \mathbb{R}^d and $\{\varphi_1, \dots, \varphi_m\} \subset \{1, \dots, d\}$ are the interpolation indices. Letting $\mathbb{P} = \Psi(\mathbf{P}^\top \Psi)^{-1} \mathbf{P}^\top$, the nonlinear term $N_r(\mathbf{x}_r(t))$ is approximated by

$$N_{h_r}(\mathbf{x}_r(t)) := \mathbf{c}^\top \mathbb{P} \mathbf{h}(\Phi \mathbf{x}_r(t)).$$

Finally, after defining the hyper-reduced Hamiltonian

$$H_{h_r}(\mathbf{x}_r(t)) = \frac{1}{2} \mathbf{x}_r(t)^\top \mathbf{Q}_r \mathbf{x}_r(t) + N_{h_r}(\mathbf{x}_r(t))$$

and using the same $\tilde{\mathbf{J}}_r$, $\tilde{\mathbf{R}}_r$ and $\tilde{\mathbf{B}}_r$ as in (6), we construct another structure-preserving ROM, denoted as the SP-G-DEIM model:

$$\begin{cases} \dot{\mathbf{x}}_r(t) = (\tilde{\mathbf{J}}_r - \tilde{\mathbf{R}}_r) \nabla_{\mathbf{x}_r} H_{h_r}(\mathbf{x}_r(t)) + \tilde{\mathbf{B}}_r \mathbf{u}(t), & (8a) \\ \mathbf{y}_r(t) = \tilde{\mathbf{B}}_r^\top \nabla_{\mathbf{x}_r} H_{h_r}(\mathbf{x}_r(t)), & (8b) \end{cases}$$

where

$$\nabla_{\mathbf{x}_r} H_{h_r}(\mathbf{x}_r(t)) = \mathbf{Q}_r \mathbf{x}_r(t) + \Phi^\top J_h^\top(\Phi \mathbf{x}_r(t)) \mathbb{P}^\top \mathbf{c}, \quad (9)$$

and we have the same initial condition as in (7). Calculating the rate of change in $H_{h_r}(\mathbf{x}_r(t))$ reveals that the dissipation inequality is satisfied at the reduced-order level. Since $\nabla_{\mathbf{x}_r} H_{h_r}(\mathbf{x}_r(t))$ is calculated with the help of interpolation, the ROM's online simulation is faster than the SP-G-ROM. For a detailed computational complexity analysis, see [29].

Notice that for both (6) and (8), in order to generate the reduced-order matrices $\tilde{\mathbf{J}}_r$, $\tilde{\mathbf{R}}_r$ and $\tilde{\mathbf{B}}_r$, the full-order matrices \mathbf{J} , \mathbf{R} and \mathbf{B} are required, hence they are intrusive approaches. However, in many real-world applications, such FOM information may not be readily available. In the next section, we introduce a nonintrusive pH-OpInf approach for constructing data-driven, structure-preserving ROMs without requiring access to the \mathbf{J} , \mathbf{R} , and \mathbf{B} matrices of the FOM.

3. Data-driven Reduced-order Models with the Port-Hamiltonian Operator Inference

To learn structure-preserving ROMs, H-OpInf in [33, 34] and GP-OpInf in [35] have been introduced for both canonical and noncanonical Hamiltonian systems, and more general gradient systems, respectively. Building on these approaches, we derive a structure-preserving ROM for the pH system (1), referred to as pH-OpInf-ROM, written in the form

$$\begin{cases} \dot{\mathbf{x}}_r(t) = (\mathbf{J}_r - \mathbf{R}_r) \nabla_{\mathbf{x}_r} H_r(\mathbf{x}_r(t)) + \mathbf{B}_r \mathbf{u}(t), & (10a) \\ \mathbf{y}_r(t) = \mathbf{B}_r^\top \nabla_{\mathbf{x}_r} H_r(\mathbf{x}_r(t)). & (10b) \end{cases}$$

While the model form is equivalent to (6), the notation is distinct to emphasize that, numerically, the projected matrices in (6) and the learned matrices in (10) are generally different. Next, we detail our approach to inferring \mathbf{J}_r , \mathbf{R}_r and \mathbf{B}_r , assuming that the functional form of the Hamiltonian is provided.

3.1. Data Reduction

Given snapshot data \mathbf{X} as in (3), as well as the input and output data

$$\mathbf{U} := [\mathbf{u}(t^0), \mathbf{u}(t^1), \dots, \mathbf{u}(t^s)] \quad \text{and} \quad \mathbf{Y} := [\mathbf{y}(t^0), \mathbf{y}(t^1), \dots, \mathbf{y}(t^s)], \quad (11)$$

we generate time derivative data by applying a finite difference operator, denoted as $\mathcal{D}_t[\cdot]$, on the state vectors:

$$\dot{\mathbf{X}} := [\mathcal{D}_t[\mathbf{x}(t^0)], \mathcal{D}_t[\mathbf{x}(t^1)], \dots, \mathcal{D}_t[\mathbf{x}(t^s)]] .$$

For instance, $\mathcal{D}_t[\cdot]$ can be chosen to be the second-order finite difference operator, satisfying

$$\mathcal{D}_t[\mathbf{x}(t^j)] = \begin{cases} (-3\mathbf{x}(t^0) + 4\mathbf{x}(t^1) - \mathbf{x}(t^2))/(2\Delta t), & j = 0, \\ (\mathbf{x}(t^{j+1}) - \mathbf{x}(t^{j-1}))/(\Delta t), & j = 1, \dots, s-1, \\ (\mathbf{x}(t^{s-2}) - 4\mathbf{x}(t^{s-1}) + 3\mathbf{x}(t^s))/(2\Delta t), & j = s. \end{cases}$$

We next compute a snapshot matrix for the gradient of the Hamiltonian function

$$\mathbf{F} := [\nabla_{\mathbf{x}}H(\mathbf{x}(t^0)), \nabla_{\mathbf{x}}H(\mathbf{x}(t^1)), \dots, \nabla_{\mathbf{x}}H(\mathbf{x}(t^s))] .$$

After finding the POD basis Φ from \mathbf{X} , we project the high-dimensional matrices onto the POD subspace and obtain the projected data

$$\mathbf{X}_r = \Phi^T \mathbf{X}, \quad \dot{\mathbf{X}}_r = \Phi^T \dot{\mathbf{X}}, \quad \text{and} \quad \mathbf{F}_r = \Phi^T \mathbf{F}. \quad (12)$$

This projection is inspired by the state equation (6a) of the SP-G-ROM. Specially, \mathbf{X}_r and $\dot{\mathbf{X}}_r$ represent the POD coefficient vectors to approximate the snapshots and associated time derivatives in the POD subspace, and \mathbf{F}_r provides an approximation of the gradient of the Hamiltonian function at the reduced-order level, following the definition of $\nabla_{\mathbf{x}_r}H_r(\mathbf{x}_r(t))$ in (5).

3.2. Two Optimization Problems for pH-OpInf

Based on these data generated from (11) and (12), one can infer \mathbf{J}_r , \mathbf{R}_r and \mathbf{B}_r for the pH-OpInf-ROM in (10) through optimization. An iterative algorithm proposed in [38] recasts the entire coefficient matrix $\begin{bmatrix} \mathbf{J}_r - \mathbf{R}_r & \mathbf{B}_r \\ -\mathbf{B}_r^T & \mathbf{0} \end{bmatrix}$ into $\tilde{\mathbf{J}} - \tilde{\mathbf{R}}$, and then learns the skew-symmetric matrix $\tilde{\mathbf{J}}$ and the symmetric and positive semi-definite matrix $\tilde{\mathbf{R}}$ iteratively. However, using the learned $\tilde{\mathbf{J}}$ and $\tilde{\mathbf{R}}$ cannot ensure that the (2,2) block in the coefficient matrix is zero with machine precision. Moreover, the iterative algorithm requires a delicate initial guess to ensure convergence. In this work, we identify the reduced operators with appropriate structural properties through a subsystem-based optimization rather than a monolithic approach.

Next, we propose and analyze two approaches. In both, we first determine \mathbf{D}_r , then post process it to obtain $\mathbf{J}_r := \frac{1}{2}(\mathbf{D}_r - \mathbf{D}_r^T)$ and $\mathbf{R}_r := -\frac{1}{2}(\mathbf{D}_r + \mathbf{D}_r^T)$ so that we again have $\mathbf{D}_r = \mathbf{J}_r - \mathbf{R}_r$.

pH-OpInf-W. We find \mathbf{D}_r and \mathbf{B}_r simultaneously by minimizing an objective function that incorporates the residuals of the state equation (10a) and the output equation (10b) at the reduced level. The residuals are balanced using a weighting parameter $\lambda_w > 0$ and we get

$$\min_{\mathbf{D}_r \in \mathbb{R}^{r \times r}, \mathbf{B}_r \in \mathbb{R}^{r \times m}} \frac{1}{2} \|\dot{\mathbf{X}}_r - \mathbf{D}_r \mathbf{F}_r - \mathbf{B}_r \mathbf{U}\|_F^2 + \frac{\lambda_w}{2} \|\mathbf{Y}^T - \mathbf{F}_r^T \mathbf{B}_r\|_F^2, \quad \text{s.t.} \quad \frac{1}{2}(\mathbf{D}_r + \mathbf{D}_r^T) \preceq \mathbf{0}. \quad (13)$$

This optimization has a semi-definite constraint and can be solved by an interior point method [42]. Operator inference implementations often use regularization terms to solve unconstrained optimization problems. However, we did not observe any additional numerical improvements for our constrained optimization in the test cases investigated in Section 5, so we did not implement regularization.

pH-OpInf-R. Since both \mathbf{Y} and \mathbf{F}_r are given, the above optimization can be split into two subtasks: finding \mathbf{B}_r by minimizing $\|\mathbf{Y}^\top - \mathbf{F}_r^\top \mathbf{B}_r\|_F^2$ in the first step, and then determining \mathbf{D}_r by minimizing $\|\dot{\mathbf{X}}_r - \mathbf{D}_r \mathbf{F}_r - \mathbf{B}_r \mathbf{U}\|_F^2$ in the second step. This leads to our second approach. First, we find \mathbf{B}_r from

$$\min_{\mathbf{B}_r \in \mathbb{R}^{r \times m}} \frac{1}{2} \|\mathbf{Y}^\top - \mathbf{F}_r^\top \mathbf{B}_r\|_F^2 + \frac{\lambda_R}{2} \|\mathbf{B}_r\|_F^2, \quad (14)$$

where $\lambda_R > 0$ is a regularization parameter; second, using the obtained \mathbf{B}_r , we optimize \mathbf{D}_r from

$$\min_{\mathbf{D}_r \in \mathbb{R}^{r \times r}} \frac{1}{2} \|\dot{\mathbf{X}}_r - \mathbf{D}_r \mathbf{F}_r - \mathbf{B}_r \mathbf{U}\|_F^2, \quad \text{s.t.} \quad \frac{1}{2} (\mathbf{D}_r + \mathbf{D}_r^\top) \preceq \mathbf{0}. \quad (15)$$

In the first step, (14) is unconstrained, and hence can be easily solved using the least-squares method, and in the second step, (15) is again a semi-definite constrained optimization, which can be solved using an interior point method.

3.3. Data-driven pH-OpInf-ROMs

In both optimization problems, since $\frac{1}{2} (\mathbf{D}_r + \mathbf{D}_r^\top) \preceq \mathbf{0}$, the inferred matrix \mathbf{R}_r must be positive semi-definite; and \mathbf{R}_r and \mathbf{J}_r are symmetric and skew symmetric, respectively, due to their definitions. After substituting them into the ROM (10), we obtain the pH-OpInf-ROMs that are structure-preserving. Following the terminology of the optimization formulations, we refer to them as pH-OpInf-W and pH-OpInf-R.

Correspondingly, after incorporating the hyper-reduction approach discussed in Section 2.2, we obtain the pH-OpInf-DEIM model:

$$\begin{cases} \dot{\mathbf{x}}_r(t) = (\mathbf{J}_r - \mathbf{R}_r) \nabla_{\mathbf{x}_r} H_{h_r}(\mathbf{x}_r(t)) + \mathbf{B}_r \mathbf{u}(t), \\ \mathbf{y}_r(t) = \mathbf{B}_r^\top \nabla_{\mathbf{x}_r} H_{h_r}(\mathbf{x}_r(t)). \end{cases} \quad (16a)$$

$$(16b)$$

In all the ROMs, the initial condition (7) is employed.

4. Error Estimates for Port-Hamiltonian Operator Inference ROMs

The numerical errors of projection-based structure-preserving ROMs have been analyzed for Hamiltonian systems in [43, 16, 29] and for pH systems in [20]. In [35], error estimates for learned Hamiltonian ROMs are provided. In this work, we continue in a similar direction and estimate the *a priori* error of the pH-OpInf-ROM approximation relative to the FOM for both the state variable and the output. To this end, we first define the Lipschitz constant and the logarithmic Lipschitz constant of a given mapping $f : \mathbb{R}^\ell \rightarrow \mathbb{R}^\ell$ as

$$C_{\text{Lip}}[f] := \sup_{\mathbf{u} \neq \mathbf{v}} \frac{\|f(\mathbf{u}) - f(\mathbf{v})\|}{\|\mathbf{u} - \mathbf{v}\|} \quad \text{and} \quad C_{\text{log-Lip}}[f] := \sup_{\mathbf{u} \neq \mathbf{v}} \frac{\langle \mathbf{u} - \mathbf{v}, f(\mathbf{u}) - f(\mathbf{v}) \rangle}{\|\mathbf{u} - \mathbf{v}\|^2},$$

where $\langle \cdot, \cdot \rangle : \mathbb{R}^\ell \times \mathbb{R}^\ell \rightarrow \mathbb{R}$ for any positive integer ℓ denotes the Euclidean inner product. The logarithmic norm [44] is defined as

$$\mu(\mathbf{A}) := \sup_{\mathbf{x} \neq \mathbf{0}} \frac{\Re(\langle \mathbf{x}, \mathbf{A} \mathbf{x} \rangle)}{\langle \mathbf{x}, \mathbf{x} \rangle},$$

where $\Re(\lambda)$ gives the real part of a complex number λ . For the state approximation error, we have the following result.

Theorem 1. Let $\mathbf{x}(t) \in \mathbb{R}^n$ be the state variable of the FOM (1) on the time interval $[0, T]$ and $\mathbf{x}_r(t) \in \mathbb{R}^r$ be the reduced-order state variable of the pH-OpInf-DEIM system (16) on the same interval. Let $\mathbf{D}_r = \mathbf{J}_r - \mathbf{R}_r$ in (16) and suppose that $\nabla_{\mathbf{x}}H(\mathbf{x})$ and $J_h(\mathbf{x})$ are both Lipschitz continuous, then the ROM state approximation error satisfies

$$\begin{aligned} \int_0^T \|\mathbf{x} - \Phi \mathbf{x}_r\|^2 dt &\leq C(T) \left(\underbrace{\int_0^T \|\mathbf{x} - \Phi \Phi^\top \mathbf{x}\|^2 dt}_{\text{projection error}} + \underbrace{\int_0^T \|\dot{\mathbf{x}} - \mathcal{D}_t[\mathbf{x}]\|^2 dt}_{\text{data error}} \right. \\ &\quad \left. + \underbrace{\int_0^T \|\Phi^\top \mathcal{D}_t[\mathbf{x}] - \mathbf{D}_r \Phi^\top \nabla_{\mathbf{x}}H(\mathbf{x}) - \mathbf{B}_r \mathbf{u}(t)\|^2 dt}_{\text{optimization error}} + \underbrace{\int_0^T \|(\mathbf{I} - \mathbb{P})J_h(\Phi \Phi^\top \mathbf{x})\|^2 dt}_{\text{hyper-reduction error}} \right), \end{aligned} \quad (17)$$

where the constant $C(T) = \max\{1 + C_2^2 T \alpha(T), C_3^2 T \alpha(T), T \alpha(T)\}$ with

$$C_1 = \mu(\Phi \mathbf{D}_r \Phi^\top \mathbf{Q}) + \|\mathbf{D}_r \Phi^\top\| C_{\text{Lip}}[\mathbf{J}_h] \|(\mathbf{P}^\top \Psi)^{-1}\| \|\mathbf{c}\|, \quad C_2 = \|\mathbf{D}_r \Phi^\top\| C_{\text{Lip}}[\nabla_{\mathbf{x}}H], \quad C_3 = \|\mathbf{D}_r\| \|\mathbf{c}\|,$$

and $\alpha(T) = 4 \int_0^T e^{2C_1(T-\tau)} d\tau$.

Four terms appear in the error bound: the first term $\int_0^T \|\mathbf{x} - \Phi \Phi^\top \mathbf{x}\|^2 dt$ measures the *projection error* caused by projecting $\mathbf{x}(t)$ onto the subspace spanned by the POD basis Φ , which has been analyzed thoroughly in [45, 46]; the second one $\int_0^T \|\dot{\mathbf{x}} - \mathcal{D}_t[\mathbf{x}]\|^2 dt$ is the *data error* caused by generating the time derivative snapshots using a finite difference scheme; the third one $\int_0^T \|\Phi^\top \mathcal{D}_t[\mathbf{x}] - \mathbf{D}_r \Phi^\top \nabla_{\mathbf{x}}H(\mathbf{x}) - \mathbf{B}_r \mathbf{u}(t)\|^2 dt$ represents the *optimization error*, which comprises the model error due to fitting the reduced-order operators \mathbf{D}_r and \mathbf{B}_r using the projected FOM data, and the numerical error arising from solving the optimization problem by numerical algorithms; and the fourth one $\int_0^T \|(\mathbf{I} - \mathbb{P})J_h(\Phi \Phi^\top \mathbf{x})\|^2 dt$ is the *hyper-reduction error* caused by the DEIM approximation of the nonlinear Jacobian, which is used to accelerate the evaluation of the gradient of reduced Hamiltonian (9). Next, we present the proof.

Proof. Consider the pH-OpInf-DEIM model (16) of a fixed dimension r , and define its approximate state error by

$$\mathbf{e}_{\mathbf{x}} := \mathbf{x} - \Phi \mathbf{x}_r,$$

which can be decomposed as $\mathbf{e}_{\mathbf{x}} = \boldsymbol{\rho} + \boldsymbol{\theta}$ with

$$\boldsymbol{\rho} := \mathbf{x} - \Phi \Phi^\top \mathbf{x}, \quad \boldsymbol{\theta} := \Phi \Phi^\top \mathbf{x} - \Phi \mathbf{x}_r.$$

After defining

$$\boldsymbol{\zeta} := \dot{\mathbf{x}} - \mathcal{D}_t[\mathbf{x}], \quad \boldsymbol{\eta} := \Phi^\top \mathcal{D}_t[\mathbf{x}] - \mathbf{D}_r \Phi^\top \nabla_{\mathbf{x}}H(\mathbf{x}) - \mathbf{B}_r \mathbf{u}(t), \quad \boldsymbol{\xi} := (\mathbf{I} - \mathbb{P})J_h(\Phi \Phi^\top \mathbf{x})\Phi$$

and using equation (16a), we have the time derivative of $\boldsymbol{\theta}$

$$\begin{aligned} \dot{\boldsymbol{\theta}} &= \Phi \Phi^\top \dot{\mathbf{x}} - \Phi \dot{\mathbf{x}}_r \\ &= (\Phi \Phi^\top \dot{\mathbf{x}} - \Phi \Phi^\top \mathcal{D}_t[\mathbf{x}]) \\ &\quad + (\Phi \Phi^\top \mathcal{D}_t[\mathbf{x}] - \Phi \mathbf{D}_r \Phi^\top \nabla_{\mathbf{x}}H(\mathbf{x}) - \Phi \mathbf{B}_r \mathbf{u}(t)) \\ &\quad + (\Phi \mathbf{D}_r \Phi^\top \nabla_{\mathbf{x}}H(\mathbf{x}) - \Phi \mathbf{D}_r \Phi^\top \nabla_{\mathbf{x}}H(\Phi \Phi^\top \mathbf{x})) \\ &\quad + (\Phi \mathbf{D}_r \Phi^\top \nabla_{\mathbf{x}}H(\Phi \Phi^\top \mathbf{x}) - \Phi \mathbf{D}_r [\Phi^\top \mathbf{Q} \Phi \Phi^\top \mathbf{x} + \Phi^\top J_h^\top(\Phi \Phi^\top \mathbf{x}) \mathbb{P}^\top \mathbf{c}]) \\ &\quad + (\Phi \mathbf{D}_r [\Phi^\top \mathbf{Q} \Phi \Phi^\top \mathbf{x} + \Phi^\top J_h^\top(\Phi \Phi^\top \mathbf{x}) \mathbb{P}^\top \mathbf{c}] - \Phi \mathbf{D}_r [\Phi^\top \mathbf{Q} \Phi \mathbf{x}_r + \Phi^\top J_h^\top(\Phi \mathbf{x}_r) \mathbb{P}^\top \mathbf{c}]). \end{aligned} \quad (18)$$

Note that

$$\frac{d}{dt} \|\boldsymbol{\theta}\| = \frac{1}{2\|\boldsymbol{\theta}\|} \frac{d}{dt} \|\boldsymbol{\theta}\|^2 = \frac{1}{\|\boldsymbol{\theta}\|} \langle \boldsymbol{\theta}, \dot{\boldsymbol{\theta}} \rangle. \quad (19)$$

By taking the inner product of equation (18) with $\boldsymbol{\theta}$, the first four terms on the right-hand side are

$$\langle \boldsymbol{\theta}, \boldsymbol{\Phi} \boldsymbol{\Phi}^\top \dot{\mathbf{x}} - \boldsymbol{\Phi} \boldsymbol{\Phi}^\top \mathcal{D}_t[\mathbf{x}] \rangle = \langle \boldsymbol{\theta}, \boldsymbol{\Phi} \boldsymbol{\Phi}^\top (\dot{\mathbf{x}} - \mathcal{D}_t[\mathbf{x}]) \rangle \leq \|\boldsymbol{\theta}\| \|\boldsymbol{\zeta}\|, \quad (20)$$

$$\langle \boldsymbol{\theta}, \boldsymbol{\Phi} \boldsymbol{\Phi}^\top \mathcal{D}_t[\mathbf{x}] - \boldsymbol{\Phi} \mathbf{D}_r \boldsymbol{\Phi}^\top \nabla_{\mathbf{x}} H(\mathbf{x}) - \boldsymbol{\Phi} \mathbf{B}_r \mathbf{u}(t) \rangle = \langle \boldsymbol{\theta}, \boldsymbol{\Phi} \boldsymbol{\eta} \rangle \leq \|\boldsymbol{\theta}\| \|\boldsymbol{\eta}\|, \quad (21)$$

$$\langle \boldsymbol{\theta}, \boldsymbol{\Phi} \mathbf{D}_r \boldsymbol{\Phi}^\top (\nabla_{\mathbf{x}} H(\mathbf{x}) - \nabla_{\mathbf{x}} H(\boldsymbol{\Phi} \boldsymbol{\Phi}^\top \mathbf{x})) \rangle \leq \|\boldsymbol{\theta}\| \|\mathbf{D}_r \boldsymbol{\Phi}^\top\| C_{\text{Lip}}[\nabla_{\mathbf{x}} H] \|\boldsymbol{\rho}\|, \quad (22)$$

$$\langle \boldsymbol{\theta}, \boldsymbol{\Phi} \mathbf{D}_r \boldsymbol{\Phi}^\top \nabla_{\mathbf{x}} H(\boldsymbol{\Phi} \boldsymbol{\Phi}^\top \mathbf{x}) - \boldsymbol{\Phi} \mathbf{D}_r [\boldsymbol{\Phi}^\top \mathbf{Q} \boldsymbol{\Phi} \boldsymbol{\Phi}^\top \mathbf{x} + \boldsymbol{\Phi}^\top J_h^\top(\boldsymbol{\Phi} \boldsymbol{\Phi}^\top \mathbf{x}) \mathbb{P}^\top \mathbf{c}] \rangle \leq \|\mathbf{D}_r\| \|\mathbf{c}\| \|\boldsymbol{\xi}\| \|\boldsymbol{\theta}\|. \quad (23)$$

For the last term, following [43, Thm. 3.1] and [29, Thm. 3.3], its linear part can be bounded by

$$\langle \boldsymbol{\theta}, \boldsymbol{\Phi} \mathbf{D}_r \boldsymbol{\Phi}^\top \mathbf{Q} (\boldsymbol{\Phi} \boldsymbol{\Phi}^\top \mathbf{x} - \boldsymbol{\Phi} \mathbf{x}_r) \rangle \leq \mu(\boldsymbol{\Phi} \mathbf{D}_r \boldsymbol{\Phi}^\top \mathbf{Q}) \|\boldsymbol{\theta}\|^2 \quad (24)$$

and the nonlinear part is bounded by

$$\langle \boldsymbol{\theta}, \boldsymbol{\Phi} \mathbf{D}_r \boldsymbol{\Phi}^\top (J_h^\top(\boldsymbol{\Phi} \boldsymbol{\Phi}^\top \mathbf{x}) - J_h^\top(\boldsymbol{\Phi} \mathbf{x}_r)) \mathbb{P}^\top \mathbf{c} \rangle \leq \|\mathbf{D}_r \boldsymbol{\Phi}^\top\| C_{\text{Lip}}[\mathbf{J}_h] \|(\mathbf{P}^\top \boldsymbol{\Psi})^{-1}\| \|\mathbf{c}\| \|\boldsymbol{\theta}\|^2. \quad (25)$$

Combining (19) with (18) and (20)-(25), we have

$$\frac{d}{dt} \|\boldsymbol{\theta}\| \leq C_1 \|\boldsymbol{\theta}\| + C_2 \|\boldsymbol{\rho}\| + C_3 \|\boldsymbol{\xi}\| + \|\boldsymbol{\zeta}\| + \|\boldsymbol{\eta}\|.$$

By the classical differential version of Gronwall lemma over the interval $[0, t]$, for any $t \in [0, T]$, we get

$$\|\boldsymbol{\theta}(t)\| \leq \int_0^t e^{C_1(t-\tau)} (C_2 \|\boldsymbol{\rho}\| + C_3 \|\boldsymbol{\xi}\| + \|\boldsymbol{\zeta}\| + \|\boldsymbol{\eta}\|) d\tau,$$

in which the fact that $\boldsymbol{\theta}(0) = \mathbf{0}$ is used, ensured by the initial condition (7). Applying the Cauchy-Schwarz inequality to the RHS and squaring both sides, we have

$$\begin{aligned} \|\boldsymbol{\theta}(t)\|^2 &\leq \int_0^t e^{2C_1(t-\tau)} d\tau \int_0^t (C_2 \|\boldsymbol{\rho}\| + C_3 \|\boldsymbol{\xi}\| + \|\boldsymbol{\zeta}\| + \|\boldsymbol{\eta}\|)^2 d\tau, \\ &\leq \alpha(T) \left(C_2^2 \int_0^T \|\boldsymbol{\rho}\|^2 dt + C_3^2 \int_0^T \|\boldsymbol{\xi}\|^2 dt + \int_0^T (\|\boldsymbol{\zeta}\|^2 + \|\boldsymbol{\eta}\|^2) dt \right), \end{aligned}$$

where $\alpha(T) = 4 \int_0^T e^{2C_1(t-\tau)} d\tau$. Hence,

$$\int_0^T \|\boldsymbol{\theta}(t)\|^2 dt \leq T \alpha(T) \left(C_2^2 \int_0^T \|\boldsymbol{\rho}\|^2 dt + C_3^2 \int_0^T \|\boldsymbol{\xi}\|^2 dt + \int_0^T (\|\boldsymbol{\zeta}\|^2 + \|\boldsymbol{\eta}\|^2) dt \right).$$

This, together with the orthogonality of $\boldsymbol{\rho}$ and $\boldsymbol{\theta}$, yields

$$\int_0^T \|\mathbf{e}_x(t)\|^2 dt \leq (1 + C_2^2 T \alpha(T)) \int_0^T \|\boldsymbol{\rho}\|^2 dt + C_3^2 T \alpha(T) \int_0^T \|\boldsymbol{\xi}\|^2 dt + T \alpha(T) \int_0^T (\|\boldsymbol{\zeta}\|^2 + \|\boldsymbol{\eta}\|^2) dt,$$

which proves the theorem. \square

Consequently, we can show the following estimate for the output approximation error.

Theorem 2. Let $\mathbf{y}(t) \in \mathbb{R}^m$ be the output of the FOM (1) on the time interval $[0, T]$ and $\mathbf{y}_r(t) \in \mathbb{R}^m$ be the output of the pH-OpInf-DEIM system (16) on the same interval. Assume that $\nabla_{\mathbf{x}}H(\mathbf{x})$ and $\mathbf{J}_h(\mathbf{x})$ are both Lipschitz continuous, then the output approximation error satisfies

$$\int_0^T \|\mathbf{y} - \mathbf{y}_r\|^2 dt \leq C \left(\underbrace{\int_0^T \|\mathbf{x} - \Phi \mathbf{x}_r\|^2 dt}_{\text{state approximation error}} + \underbrace{\int_0^T \|\mathbf{y} - \mathbf{B}_r^T \Phi^T \nabla_{\mathbf{x}}H(\mathbf{x})\|^2 dt}_{\text{optimization error}} + \underbrace{\int_0^T \|(\mathbf{I} - \mathbb{P})J_h(\Phi \Phi^T \mathbf{x})\Phi\|^2 dt}_{\text{hyper-reduction error}} \right), \quad (26)$$

where $C = 4 \max\{1, C_4^2, C_5^2, C_6^2\}$ with the constants

$$C_4 = \|\mathbf{B}_r^T \Phi^T\| C_{\text{Lip}}[\nabla_{\mathbf{x}}H], \quad C_5 = \|\mathbf{B}_r\| \|\mathbf{c}\|, \quad \text{and} \quad C_6 = \|\mathbf{B}_r^T \Phi^T\| \left(\|\mathbf{Q}\| + C_{\text{Lip}}[J_h] \|(\mathbf{P}^T \Psi)^{-1}\| \|\mathbf{c}\| \right).$$

Three terms appear in this error bound: the first term $\int_0^T \|\mathbf{x} - \Phi \mathbf{x}_r\|^2 dt$ represents the *state approximation error*, which is estimated in Theorem 1; the second one $\int_0^T \|\mathbf{y} - \mathbf{B}_r^T \Phi^T \nabla_{\mathbf{x}}H(\mathbf{x})\|^2 dt$ is the *optimization error* caused by inferring \mathbf{B}_r from the optimization problems; and the third one $\int_0^T \|(\mathbf{I} - \mathbb{P})J_h(\Phi \Phi^T \mathbf{x})\Phi\|^2 dt$ is the same *hyper-reduction error* due to the DEIM interpolation of the nonlinear Jacobian of the reduced Hamiltonian. Next, we present the proof.

Proof. Consider the pH-OpInf-DEIM model (16) of a fixed dimension r , and define its output approximation error by

$$\mathbf{e}_y := \mathbf{y} - \mathbf{y}_r.$$

By equation (16b), it can be equivalently rewritten as

$$\begin{aligned} \mathbf{e}_y &= \mathbf{y} - \mathbf{B}_r^T \nabla_{\mathbf{x}} H_{h_r}(\mathbf{x}_r) \\ &= \mathbf{y} - \mathbf{B}_r^T \Phi^T \nabla_{\mathbf{x}} H(\mathbf{x}) \\ &\quad + \mathbf{B}_r^T \Phi^T \nabla_{\mathbf{x}} H(\mathbf{x}) - \mathbf{B}_r^T \Phi^T \nabla_{\mathbf{x}} H(\Phi \Phi^T \mathbf{x}) \\ &\quad + \mathbf{B}_r^T [\Phi^T \mathbf{Q} \Phi \Phi^T \mathbf{x} + \Phi^T J_h^T(\Phi \Phi^T \mathbf{x}) \mathbf{c}] - \mathbf{B}_r^T [\Phi^T \mathbf{Q} \Phi \Phi^T \mathbf{x} + \Phi^T J_h^T(\Phi \Phi^T \mathbf{x}) \mathbb{P}^T \mathbf{c}] \\ &\quad + \mathbf{B}_r^T [\Phi^T \mathbf{Q} \Phi \Phi^T \mathbf{x} + \Phi^T J_h^T(\Phi \Phi^T \mathbf{x}) \mathbb{P}^T \mathbf{c}] - \mathbf{B}_r^T [\Phi^T \mathbf{Q} \Phi \mathbf{x}_r + \Phi^T J_h^T(\Phi \mathbf{x}_r) \mathbb{P}^T \mathbf{c}]. \end{aligned} \quad (27)$$

Defining

$$\boldsymbol{\varphi} := \mathbf{y} - \mathbf{B}_r^T \Phi^T \nabla_{\mathbf{x}} H(\mathbf{x}), \quad \boldsymbol{\rho} := \mathbf{x} - \Phi \Phi^T \mathbf{x}, \quad \boldsymbol{\xi} := (\mathbf{I} - \mathbb{P})J_h(\Phi \Phi^T \mathbf{x})\Phi, \quad \boldsymbol{\theta} := \Phi \Phi^T \mathbf{x} - \Phi \mathbf{x}_r,$$

we then have

$$\|\mathbf{e}_y\| \leq \|\boldsymbol{\varphi}\| + C_4 \|\boldsymbol{\rho}\| + C_5 \|\boldsymbol{\xi}\| + C_6 \|\boldsymbol{\theta}\|,$$

for any $t \in [0, T]$. Hence,

$$\|\mathbf{e}_y\|^2 \leq 4 \left(C_4^2 \|\boldsymbol{\rho}\|^2 + C_6^2 \|\boldsymbol{\theta}\|^2 + \|\boldsymbol{\varphi}\|^2 + C_5^2 \|\boldsymbol{\xi}\|^2 \right).$$

After integrating both sides from 0 to T , using $\mathbf{e}_x = \boldsymbol{\rho} + \boldsymbol{\theta}$ and the orthogonality of $\boldsymbol{\rho}$ and $\boldsymbol{\theta}$, we get

$$\int_0^T \|\mathbf{e}_y\|^2 dt \leq 4 \left(\max(C_4^2, C_6^2) \int_0^T \|\mathbf{e}_x\|^2 dt + \int_0^T \|\boldsymbol{\psi}\|^2 dt + C_5^2 \int_0^T \|\boldsymbol{\xi}\|^2 dt \right).$$

This proves the theorem. \square

When hyper-reduction is not applied, the pH-OpInf-DEIM model coincides with the pH-OpInf-ROM, and we have the following result.

Corollary 2.1. *Let $\mathbf{x}(t)$ and $\mathbf{y}(t)$ be the state and output of the FOM (1), respectively, on the time interval $[0, T]$ and $\mathbf{x}_r(t)$ and $\mathbf{y}_r(t)$ be the reduced-order state and output, respectively, of the pH-OpInf-ROM defined in (10) over the same interval. Let $\mathbf{D}_r = \mathbf{J}_r - \mathbf{R}_r$ in (10) and suppose that $\nabla_{\mathbf{x}}H(\mathbf{x})$ and $J_h(\mathbf{x})$ are both Lipschitz continuous, then the ROM state approximation error satisfies*

$$\int_0^T \|\mathbf{x} - \Phi \mathbf{x}_r\|^2 dt \leq \widehat{C}(T) \left(\underbrace{\int_0^T \|\mathbf{x} - \Phi \Phi^\top \mathbf{x}\|^2 dt}_{\text{projection error}} + \underbrace{\int_0^T \|\dot{\mathbf{x}} - \mathcal{D}_t[\mathbf{x}]\|^2 dt}_{\text{data error}} + \underbrace{\int_0^T \|\Phi^\top \mathcal{D}_t[\mathbf{x}] - \mathbf{D}_r \Phi^\top \nabla_{\mathbf{x}}H(\mathbf{x}) - \mathbf{B}_r \mathbf{u}(t)\|^2 dt}_{\text{optimization error}} \right), \quad (28)$$

where the constant $\widehat{C}(T) = \max\{1 + C_8^2 T \alpha(T), T \alpha(T)\}$ with

$$C_7 = C_{\log\text{-Lip}}[\Phi \mathbf{D}_r \Phi^\top \nabla_{\mathbf{x}}H], \quad C_8 = \|\mathbf{D}_r \Phi^\top\| C_{\text{Lip}}[\nabla_{\mathbf{x}}H], \quad \text{and} \quad \alpha(T) = 3 \int_0^T e^{2C_7(T-\tau)} d\tau.$$

The corresponding output approximation error satisfies

$$\int_0^T \|\mathbf{y} - \mathbf{y}_r\|^2 dt \leq \widehat{C} \left(\underbrace{\int_0^T \|\mathbf{x} - \Phi \mathbf{x}_r\|^2 dt}_{\text{state approximation error}} + \underbrace{\int_0^T \|\mathbf{y} - \mathbf{B}_r^\top \Phi^\top \nabla_{\mathbf{x}}H(\mathbf{x})\|^2 dt}_{\text{optimization error}} \right), \quad (29)$$

where the constant $\widehat{C} = 2 \max\{1, C_9^2\}$ with $C_9 = \|\mathbf{B}_r^\top \Phi^\top\| C_{\text{Lip}}[\nabla_{\mathbf{x}}H]$.

Proof. Following the same steps outlined in Theorem 1 but replacing inequalities (23), (24), and (25) with the inequality

$$\langle \theta, \Phi \mathbf{D}_r \Phi^\top (\nabla_{\mathbf{x}}H(\Phi \Phi^\top \mathbf{x}) - \nabla_{\mathbf{x}}H(\Phi \mathbf{x}_r)) \rangle \leq \|\theta\| C_{\log\text{-Lip}}[\Phi \mathbf{D}_r \Phi^\top \nabla_{\mathbf{x}}H] \|\theta\|,$$

we obtain the state approximation error in (28). Then using the same argument as in Theorem 2 and changing the equation (27) to

$$\mathbf{e}_y = \mathbf{y} - \mathbf{B}_r^\top \nabla_{\mathbf{x}_r} H_r(\mathbf{x}_r) = \mathbf{y} - \mathbf{B}_r^\top \Phi^\top \nabla_{\mathbf{x}}H(\mathbf{x}) + \mathbf{B}_r^\top \Phi^\top \nabla_{\mathbf{x}}H(\mathbf{x}) - \mathbf{B}_r^\top \Phi^\top \nabla_{\mathbf{x}}H(\Phi \mathbf{x}_r),$$

we obtain the inequality

$$\|\mathbf{e}_y\| \leq \|\varphi\| + \|\mathbf{B}_r^\top \Phi^\top\| C_{\text{Lip}}[\nabla_{\mathbf{x}}H] \|\mathbf{e}_x\|,$$

and further the output approximation error in (29). This completes the proof. \square

Remark 1. The re-projection method has been introduced in [47] to reduce optimization errors for operator inference. When the FOM drift terms are polynomial and the time derivative data is discretized in the same manner as the FOM, the re-projection approach ensures that the inferred ROM recovers the intrusive Galerkin-projection ROM and the optimization error is zero. However, this does not hold for port-Hamiltonian systems. Suppose the re-projection method generates a sequence of approximate state vectors

$\{\tilde{\mathbf{x}}_0, \tilde{\mathbf{x}}_1, \dots, \tilde{\mathbf{x}}_s\}$, in which $\tilde{\mathbf{x}}_{n+1}$ is obtained from (1a) after approximating the time derivative by \mathcal{D}_t and taking $\tilde{\mathbf{x}}_n$ as the initial data. Then it satisfies

$$\mathcal{D}_t[\Phi^\top \tilde{\mathbf{x}}_n] = \Phi^\top \mathbf{D} \nabla_{\mathbf{x}} H(\Phi \Phi^\top \tilde{\mathbf{x}}_n) + \Phi^\top \mathbf{B} \mathbf{u}_n. \quad (30)$$

Define $\tilde{\mathbf{X}} := \Phi \Phi^\top [\tilde{\mathbf{x}}_0, \tilde{\mathbf{x}}_1, \dots, \tilde{\mathbf{x}}_s] \in \mathbb{R}^{r \times (s+1)}$. Assuming that $\mathbf{B}_r = \Phi^\top \mathbf{B}$ has been obtained, we next find $\mathbf{D}_r \in \mathbb{R}^{r \times r}$ by minimizing

$$\frac{1}{2} \left\| \Phi^\top \mathcal{D}_t [\tilde{\mathbf{X}}] - \mathbf{D}_r \Phi^\top \nabla_{\mathbf{x}} H(\tilde{\mathbf{X}}) - \mathbf{B}_r \mathbf{U} \right\|_F^2 \quad \text{s.t.} \quad \frac{1}{2} (\mathbf{D}_r + \mathbf{D}_r^\top) \preceq \mathbf{0}.$$

Because of the relation in (30) and $\mathcal{D}_t[\Phi^\top \tilde{\mathbf{X}}] = \Phi^\top \mathcal{D}_t[\tilde{\mathbf{X}}]$, it is equivalent to minimize

$$\frac{1}{2} \left\| \Phi^\top \mathbf{D} \nabla_{\mathbf{x}} H(\tilde{\mathbf{X}}) - \mathbf{D}_r \Phi^\top \nabla_{\mathbf{x}} H(\tilde{\mathbf{X}}) \right\|_F^2 \quad \text{s.t.} \quad \frac{1}{2} (\mathbf{D}_r + \mathbf{D}_r^\top) \preceq \mathbf{0}.$$

In general, the minimizer \mathbf{D}_r solved from the optimization can not reduce the objective function to zero.

5. Numerical Experiments

In this section, we provide two numerical experiments to demonstrate the effectiveness and qualitative features of the proposed method. In Section 5.1 we define the error metrics used to evaluate the quality and accuracy of the pH-OpInf-ROM and the pH-OpInf-DEIM model. A *linear* mass-spring-damper system [48, 38] is studied in Section 5.2. As the system lacks a nonlinearity, the pH-OpInf-ROM will be applied and investigated. The *nonlinear* Toda lattice model [20], which describes a chain of particles with exponential interactions between neighboring particles, is tested in Section 5.3. Due to nonlinearities in this system, the pH-OpInf-DEIM model will be employed and tested.

5.1. Error Measures

To test the ROMs' accuracy, we compute the reduced-order approximation errors for both state variable \mathbf{x} and output \mathbf{y} , as functions of the dimension r of the ROMs:

$$\mathcal{E}_{\mathbf{x}}(r) := \sqrt{\frac{T}{N} \sum_{k=1}^N \|\mathbf{x}(t^k) - \Phi \mathbf{x}_r(t^k)\|^2}, \quad (31)$$

$$\mathcal{E}_{\mathbf{y}}(r) := \sqrt{\frac{T}{N} \sum_{k=1}^N \|\mathbf{y}(t^k) - \mathbf{y}_r(t^k)\|^2}, \quad (32)$$

where $\mathbf{x}(t^k)$, $\mathbf{y}(t^k)$ are full-order solutions and $\mathbf{x}_r(t^k)$, $\mathbf{y}_r(t^k)$ are reduced-order solutions, for $k = 1, 2, \dots, N$, and Φ is the POD basis matrix. To further illustrate the error analysis in (17) and (26), we evaluate the

projection error, optimization error and hyper-reduction error as

$$\mathcal{E}_{\text{proj}_x}(r) := \sqrt{\frac{T}{N} \sum_{k=1}^N \|\mathbf{x}(t^k) - \Phi\Phi^\top \mathbf{x}(t^k)\|^2}, \quad (33)$$

$$\mathcal{E}_{\text{proj}_{\nabla H}}(r) := \sqrt{\frac{T}{N} \sum_{k=1}^N \|\nabla_{\mathbf{x}} H(\mathbf{x}(t^k)) - \Phi\Phi^\top \nabla_{\mathbf{x}} H(\mathbf{x}(t^k))\|^2}, \quad (34)$$

$$\mathcal{E}_{\text{opt}_x}(r) := \sqrt{\frac{T}{N} \sum_{k=1}^N \|\Phi^\top \mathcal{D}_t[\mathbf{x}(t^k)] - (\mathbf{J}_r - \mathbf{R}_r)\Phi^\top \nabla_{\mathbf{x}} H(\mathbf{x}(t^k)) - \mathbf{B}_r \mathbf{u}(t^k)\|^2}, \quad (35)$$

$$\mathcal{E}_{\text{opt}_y}(r) := \sqrt{\frac{T}{N} \sum_{k=1}^N \|\mathbf{y}(t^k) - \mathbf{B}_r^\top \Phi^\top \nabla_{\mathbf{x}} H(\mathbf{x}(t^k))\|^2}, \quad (36)$$

$$\mathcal{E}_{\text{DEIM}}(r) := \sqrt{\frac{T}{N} \sum_{k=1}^N \|(\mathbf{I} - \mathbb{P})J_h(\Phi\Phi^\top \mathbf{x}(t^k))\Phi\|^2}. \quad (37)$$

In numerical tests, the FOM solutions are simulated in the time interval $[0, T_{\text{FOM}}]$, while $[0, T_{\text{ROM}}]$ in the ROM simulations. Furthermore, we utilize the optimization software MOSEK [49], under an academic license, to solve the optimization problems via the open-source CVXPY library [50, 51].

5.2. Linear Case: Mass-Spring-Damper System

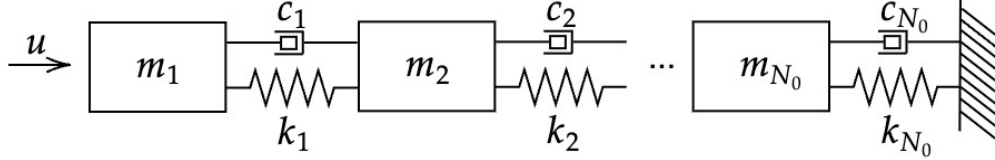


Figure 1: The Mass-Spring-Damper System.

In our first experiment, we consider the linear mass-spring-damper system, illustrated in Figure 1, consisting of masses m_i , springs with constants k_i and dampers with non-negative damping constants c_i for $i = 1, 2, \dots, N_0$. The input $u(t)$ is the external force exerted on the first mass m_1 and the output $y(t)$ is the velocity of the first mass. The state vector $\mathbf{x} = [q_1, p_1, \dots, q_{N_0}, p_{N_0}] \in \mathbb{R}^{2N_0}$, where q_i and p_i represent the displacement and momentum of the i th mass, respectively. The system is governed by (1) with Hamiltonian $H(\mathbf{x}) = \frac{1}{2} \mathbf{x}^\top \mathbf{Q} \mathbf{x}$. For instance, when $N_0 = 3$, we have

$$\mathbf{J} = \begin{bmatrix} 0 & 1 & 0 & 0 & 0 & 0 \\ -1 & 0 & 0 & 0 & 0 & 0 \\ 0 & 0 & 0 & 1 & 0 & 0 \\ 0 & 0 & -1 & 0 & 0 & 0 \\ 0 & 0 & 0 & 0 & 0 & 1 \\ 0 & 0 & 0 & 0 & -1 & 0 \end{bmatrix}, \quad \mathbf{Q} = \begin{bmatrix} k_1 & 0 & k_1 & 0 & 0 & 0 \\ 0 & \frac{1}{m_1} & 0 & 0 & 0 & 0 \\ -k_1 & 0 & k_1 + k_2 & 0 & -k_2 & 0 \\ 0 & 0 & 0 & \frac{1}{m_2} & 0 & 0 \\ 0 & 0 & -k_2 & 0 & k_2 + k_3 & 0 \\ 0 & 0 & 0 & 0 & 0 & \frac{1}{m_3} \end{bmatrix},$$

$$\mathbf{R} = \text{diag}(0, c_1, 0, c_2, 0, c_3), \quad \text{and} \quad \mathbf{B}^\top = [0 \ 1 \ 0 \ 0 \ 0 \ 0].$$

Problem and computational setting. We set $\mathbf{x}_0 = \mathbf{0}$, $N_0 = 100$, $m_i = 4$, $k_i = 4$ and $c_i = 1$ for $i = 1, 2, \dots, 100$, and choose the input of the system to be $u(t) = \exp(-\frac{t}{2}) \sin(t^2)$. For the full-order simulation, we set $T_{\text{FOM}} = 10$ and use the implicit midpoint rule for time integration with a step size $\Delta t = 0.01$.

After constructing the snapshot matrices \mathbf{X} , \mathbf{Y} , and \mathbf{U} , and generating the reduced basis matrix $\mathbf{\Phi} \in \mathbb{R}^{n \times r}$, which consists of the r leading left singular vectors of \mathbf{X} , we apply pH-OpInf-W and pH-OpInf-R to infer \mathbf{J}_r , \mathbf{R}_r and \mathbf{B}_r , as described in Section 3. Since selecting appropriate hyper-parameters, λ_W and λ_R , is crucial for the optimization, we next investigate the effects of these optimization parameters.

Test 1. Effects of optimization parameters

First, we study the influence of the weight parameter λ_W in the optimization problem (13) on the quality of the pH-OpInf-W. Note that, in (13), λ_W serves as a balancing factor between the two error components, $\mathcal{E}_{\text{opt}_x}$ and $\mathcal{E}_{\text{opt}_y}$, in the minimization process. We vary the reduced dimension r from 5, 10, 15 to 20 and test eight values for λ_W from the set $\{10^0, 10^1, \dots, 10^7\}$, for each value of r . Figure 2 shows the corresponding optimization errors. As λ_W increases up to 10^5 , the optimization error $\mathcal{E}_{\text{opt}_x}$ remains nearly unchanged for all r , while $\mathcal{E}_{\text{opt}_y}$ decreases. Beyond this point, $\mathcal{E}_{\text{opt}_y}$ either decays or levels off, while $\mathcal{E}_{\text{opt}_x}$ remains nearly unchanged for $r = 5, 10, 15$, but increases for $r = 20$. Therefore, $\lambda_W = 10^5$ is selected in the rest of the experiments.

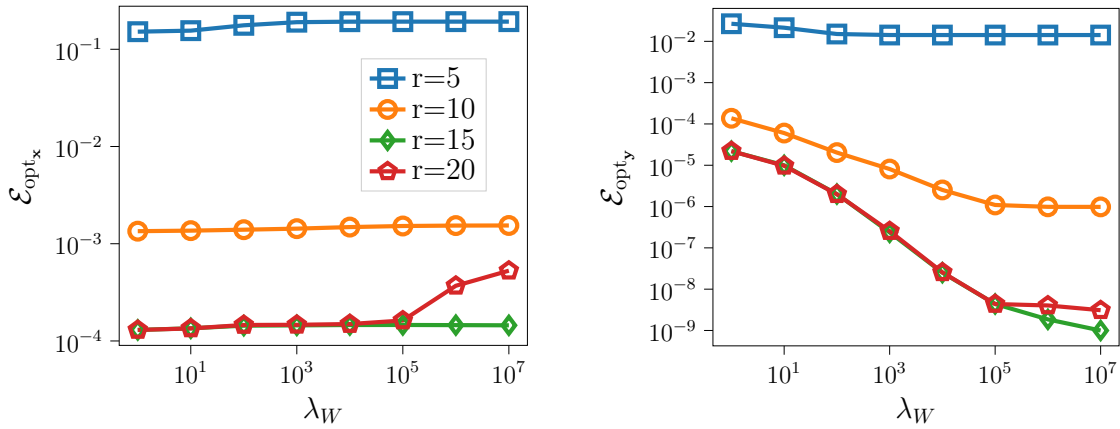


Figure 2: Mass-Spring-Damper System: Optimization errors by pH-OpInf-W of r dimensions using different values of λ_W : $\mathcal{E}_{\text{opt}_x}$ (left) and $\mathcal{E}_{\text{opt}_y}$ (right).

Next, we test the influence of the regularization parameter λ_R on the optimization problem and the resulting effects on the pH-OpInf-R ROM. When $\lambda_R = 0$, we find that the solution \mathbf{B}_r from equation (14) using least squares is poorly conditioned, leading to unstable ROM simulations. Taking $r = 5, 10, 15$ and 20 and selecting eight values of λ_R from the set $\{10^{-14}, 10^{-13}, \dots, 10^{-7}\}$, we solve (14) and (15), respectively. The optimization errors $\mathcal{E}_{\text{opt}_x}$ and $\mathcal{E}_{\text{opt}_y}$ are shown in Figure 3. For $r = 5$ and 10 , the optimization errors are relatively steady as λ_R varies. However, for larger values of $r = 15$ and 20 , as λ_R increases, both $\mathcal{E}_{\text{opt}_x}$ and $\mathcal{E}_{\text{opt}_y}$ initially decrease (with $\mathcal{E}_{\text{opt}_x}$ remaining unchanged for $r = 15$), but after $\lambda_R = 10^{-11}$, both begin to increase. Therefore, in subsequent experiments, we select $\lambda_R = 10^{-11}$ in pH-OpInf-R.

For pH-OpInf-W with $\lambda_W = 10^5$ and pH-OpInf-R with $\lambda_R = 10^{-11}$, the minimum eigenvalues of the obtained \mathbf{R}_r are listed in Table 1 for $r = 5, 10, 15$ and 20 , which demonstrates the positive semi-definiteness of the obtained \mathbf{R}_r .

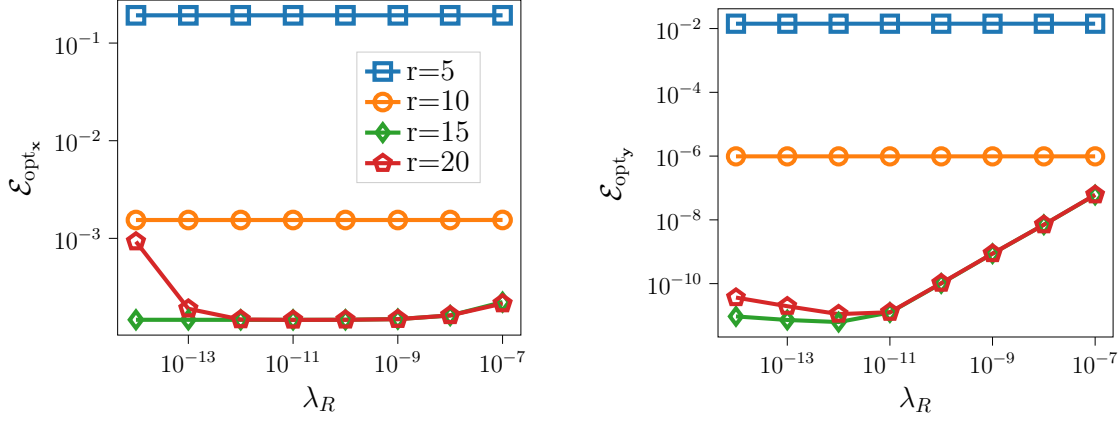


Figure 3: Mass-Spring-Damper System: Optimization errors by pH-OpInf-R of r dimensions using different values of λ_R : $\mathcal{E}_{\text{opt}_x}$ (left) and $\mathcal{E}_{\text{opt}_y}$ (right).

Table 1: Mass-Spring-Damper System: Minimum eigenvalues of \mathbf{R}_r obtained by pH-OpInf-W and pH-OpInf-R for different values of r .

	$r=5$	$r=10$	$r=15$	$r=20$
pH-OpInf-W	1.460×10^{-5}	7.864×10^{-7}	7.729×10^{-5}	9.396×10^{-5}
pH-OpInf-R	5.486×10^{-8}	2.807×10^{-6}	3.567×10^{-5}	4.682×10^{-5}

Test 2. Illustration of the error estimates

Based on Corollary 2.1, for this linear system, the state error is bounded by the sum of projection error, data error, and optimization error; and the output error is bounded by the state approximation error and the corresponding optimization error. Next, we illustrate the error estimates for the pH-OpInf-ROM (10), generated using the inferred reduced operators from either pH-OpInf-W or pH-OpInf-R, and compare the approximation errors with those of the intrusive SP-G-ROM of the same dimensions. To this end, we choose $\Delta t = 10^{-3}$ such that the data error is negligible relative to other sources of error.

Setting $T_{\text{FOM}} = T_{\text{ROM}} = 10$ and gradually increasing the ROM dimension r by 5, from 5 to 50, we simulate the pH-OpInf-ROMs. In this case, the singular values of the snapshot matrix \mathbf{X} decay quickly: the first 5 POD modes capture 95.24% of the snapshot energy, while the first 10 modes capture 99.99%. The associated numerical errors defined in (31)–(36) are plotted in Figure 4: the left column corresponds to pH-OpInf-W, and the right column corresponds to pH-OpInf-R. Note that the magnitude of the state vectors is 0.661, while that of the output is 0.083. From the top row, we observe that in both cases, the projection error $\mathcal{E}_{\text{proj}_x}$ continues to decay as r increases, eventually reaching the machine precision beyond $r = 25$. Meanwhile, the optimization error $\mathcal{E}_{\text{opt}_x}$ decreases to around 10^{-5} as r increases to 20 and remains nearly steady. Consequently, the state approximation error \mathcal{E}_x is dominated by $\mathcal{E}_{\text{opt}_x}$ and exhibits similar behavior. From the middle row, we find that the optimization error $\mathcal{E}_{\text{opt}_y}$ from pH-OpInf-R is smaller than that from pH-OpInf-W when $r > 5$, but in both cases, $\mathcal{E}_{\text{opt}_y}$ is much smaller than the state approximation error \mathcal{E}_x . Thus, the output approximation error \mathcal{E}_y is dominated by \mathcal{E}_x and displays similar behavior. In the bottom row, \mathcal{E}_y from the pH-OpInf-ROMs is compared with that of the SP-G-ROM. The pH-OpInf-ROM, based on either pH-OpInf-W or pH-OpInf-R, attains better results when $r < 25$. Beyond that, SP-G-ROM achieves better approximations. Therefore, in case when the computation budget is a concern, a ROM with a lower dimension is preferable, and the pH-OpInf-ROM is the better choice. Furthermore, the time evolution

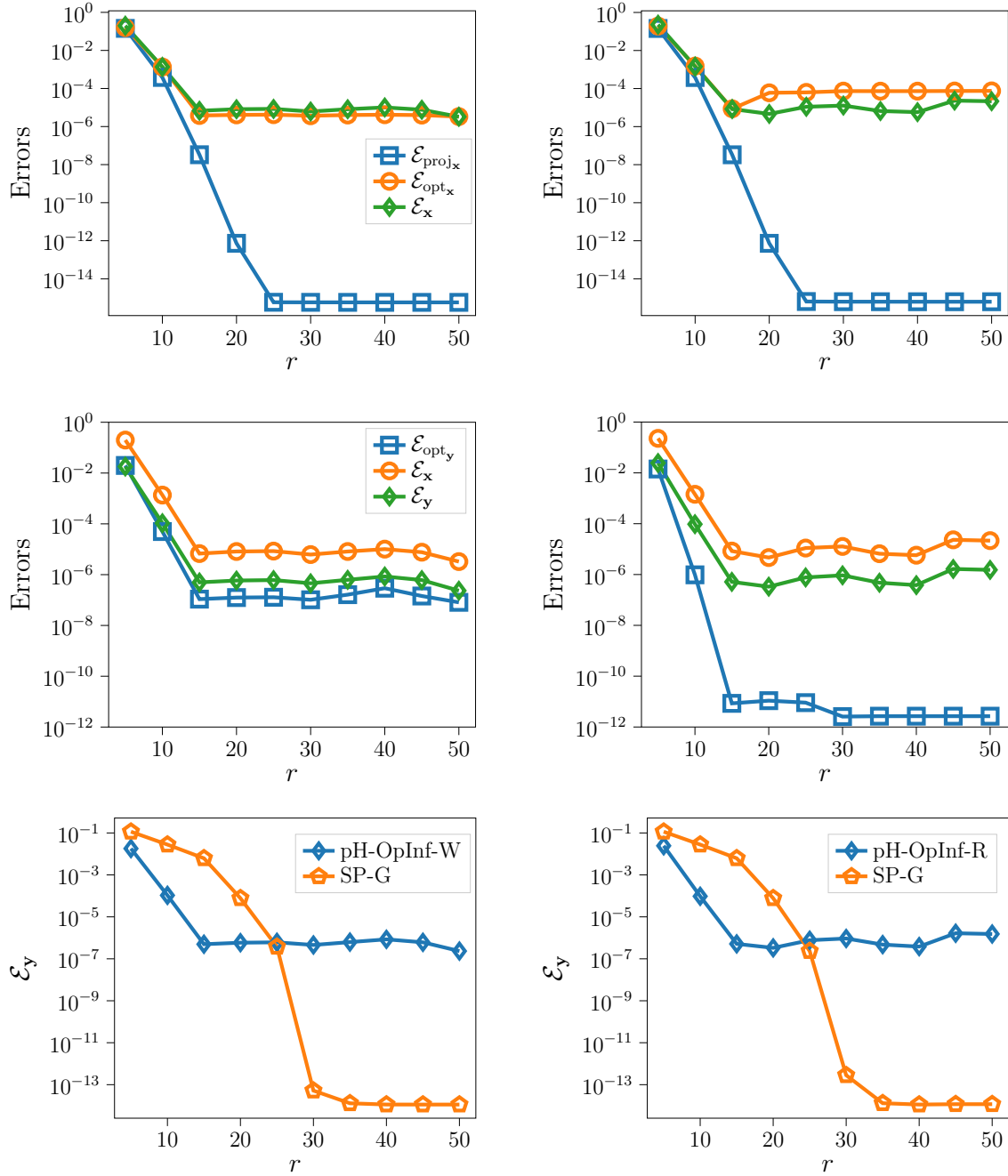


Figure 4: Mass-Spring-Damper System: Numerical errors of pH-OpInf-W (left) and pH-OpInf-R (right) of r dimensions when $T_{\text{FOM}} = T_{\text{ROM}} = 10$.

of the output and approximate Hamiltonian from the pH-OpInf-ROMs is shown in Figure 5. We observe that the reduced-order approximations of both the output and the Hamiltonian, using either pH-OpInf-W or pH-OpInf-R, closely match those from the FOM simulation when $r \geq 10$.

Overall, the pH-OpInf-ROM constructed using reduced operators from either optimization problem pro-

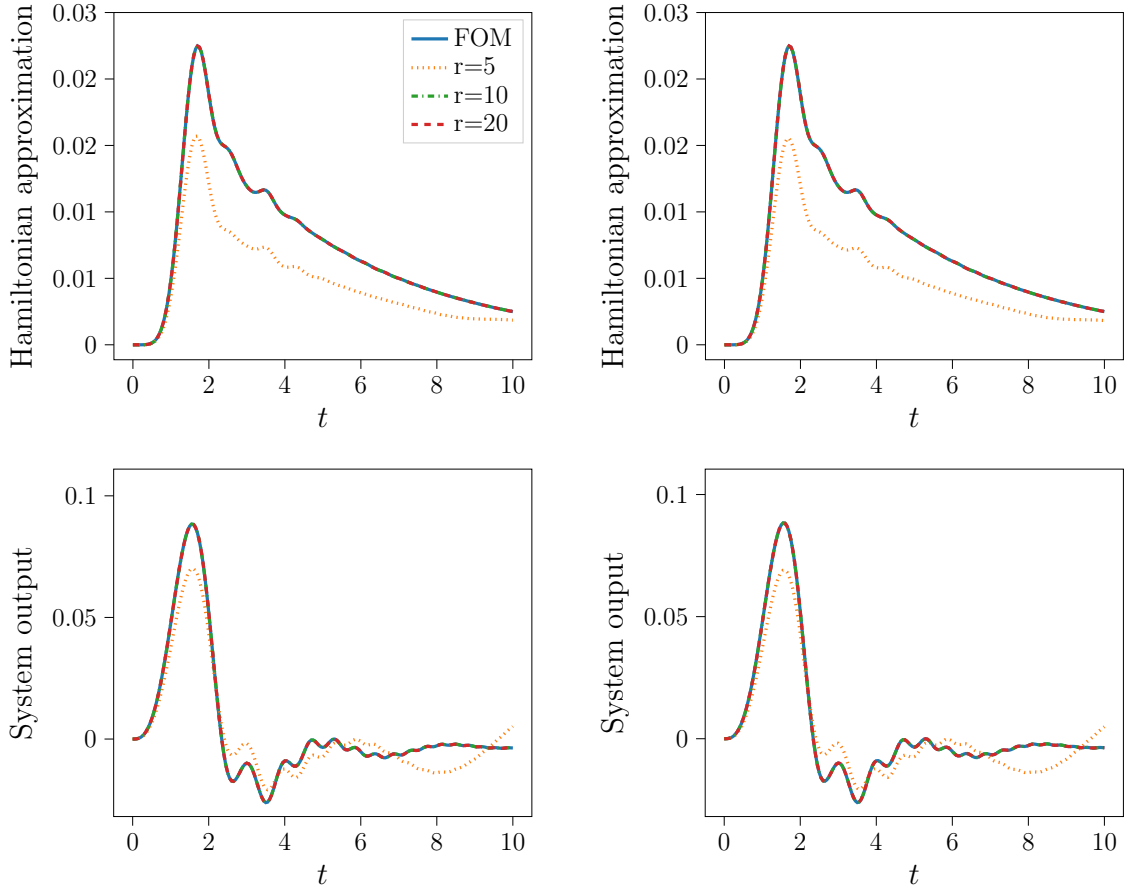


Figure 5: Mass-Spring-Damper System: Hamiltonian approximation (top row) and system output (bottom row) from pH-OpInf-W (left) and pH-OpInf-R (right) of r dimensions, along with those of the FOM. All subplots share the same legend shown in the first one.

vides good approximations. However, compared to pH-OpInf-W, the pH-OpInf-R achieves a smaller optimization error for the output. Therefore, we use pH-OpInf-R in the next experiment.

Test 3. Performance at a different input

We test the pH-OpInf-ROM using an input different from the one used to generate the training snapshots. To infer the reduced operator, we use the data associated with the training input $u(t) = \exp(-\frac{t}{2}) \sin(t^2)$ as shown in Figure 6 (left), which has increasing frequency to excite the model. After building the ROM with $r = 20$ dimensions, we test it using a different input u , shown in Figure 6 (right). The sawtooth signal is a challenging test case, as it is discontinuous. The corresponding output and Hamiltonian function from the FOM and ROM simulations are shown in Figure 7. The results indicate that the pH-OpInf-ROM performs well, as both the reduced-order output and the Hamiltonian function closely match the FOM results.

5.3. Nonlinear Case: Toda Lattice Model

We consider the nonlinear Toda lattice model, which describes the motion of a chain of particles, each one connects to its nearest neighbors with ‘exponential springs’. The equations of motion for the N_0 -particle

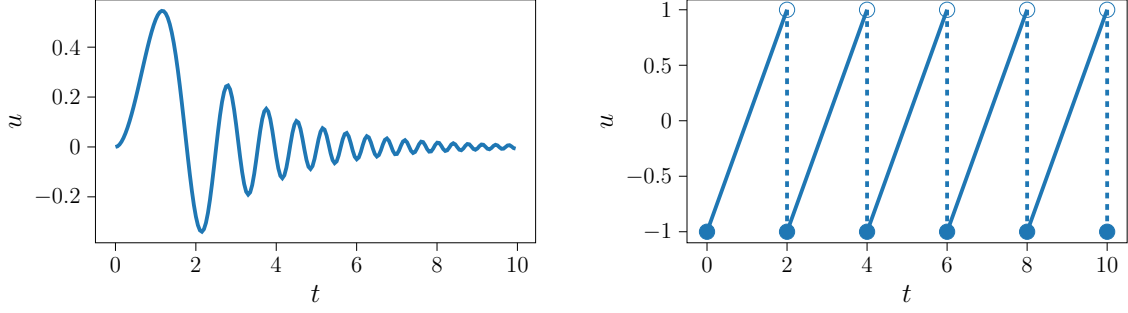


Figure 6: Mass-Spring-Damper System: Training input (left) and testing input (right) for Test 3.

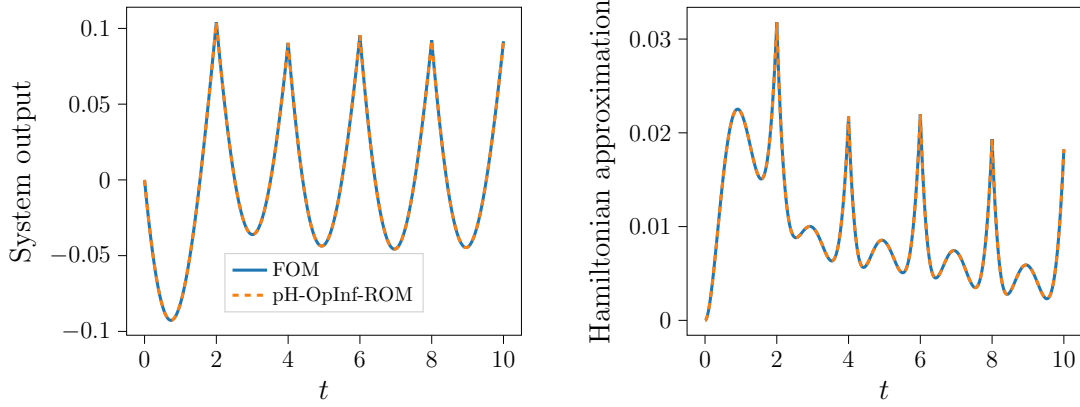


Figure 7: Mass-Spring-Damper System: Simulation results of pH-OpInf-ROM for $r = 20$ and the FOM: system output (left) and Hamiltonian approximation (right) for Test 3.

Toda lattice with such exponential interactions can be written in the form of a nonlinear pH system as in (1) with

$$\mathbf{J} = \begin{bmatrix} \mathbf{0} & \mathbf{I} \\ -\mathbf{I} & \mathbf{0} \end{bmatrix}_{n \times n}, \quad \mathbf{R} = \begin{bmatrix} \mathbf{0} & \mathbf{0} \\ \mathbf{0} & \text{diag}(\gamma_1, \dots, \gamma_{N_0}) \end{bmatrix}_{n \times n}, \quad \text{and} \quad \mathbf{B} = \begin{bmatrix} \mathbf{0} \\ \mathbf{e}_1 \end{bmatrix}_{n \times 1},$$

where $\mathbf{e}_1 = [1, 0, \dots, 0]_{N_0}^\top$, $n = 2N_0$, γ_j represents damping coefficients associated with the j th particle in the system and

$$\mathbf{x} = \begin{bmatrix} \mathbf{q} \\ \mathbf{p} \end{bmatrix}_{n \times 1}, \quad \mathbf{q} = [q_1, \dots, q_{N_0}]^\top \text{ and } \mathbf{p} = [p_1, \dots, p_{N_0}]^\top,$$

with q_j and p_j , for $j = 1, \dots, N_0$, being the displacement of the j th particle from its equilibrium position and the momentum, respectively. The associated Hamiltonian function is nonlinear, given by

$$H(\mathbf{x}) = \sum_{k=1}^{N_0} \frac{1}{2} p_k^2 + \sum_{k=1}^{N_0-1} \exp(q_k - q_{k+1}) + \exp(q_{N_0}) - q_1 - N_0. \quad (38)$$

Problem and computational setting. We set $\mathbf{x}_0 = \mathbf{0}$, $N_0 = 1000$, and $\gamma_j = 0.1$ for $j = 1, \dots, N_0$. The system is excited by the input $u(t) = 0.1 \sin(t)$. In the full-order simulation with the final time $T_{\text{FOM}} = 50$, we use the implicit midpoint rule with the time step size $\Delta t = 0.01$ for time integration. The reduced operators

\mathbf{J}_r , \mathbf{R}_r and \mathbf{B}_r are then inferred as described in Section 3 through either pH-OpInf-W or pH-OpInf-R. Next, we investigate the effects of the optimization parameters λ_W and λ_R in the optimization problems.

Test 1. Effects of optimization parameters

We analyze the effect of the weight parameter λ_W in the optimization problem (13) on the quality of the pH-OpInf-W ROM, by taking reduced dimensions $r = 20, 40, 60$ and 80 and testing eight values of λ_W from the set $\{10^0, 10^1, \dots, 10^7\}$. Figure 8 illustrates the optimization errors $\mathcal{E}_{\text{opt}_x}$ (left) and $\mathcal{E}_{\text{opt}_y}$ (right) for varying λ_W and r . When r is small, variations in λ_W have a minimal impact on the optimization. However, for larger dimensions ($r = 60$ and 80), increasing λ_W reduces $\mathcal{E}_{\text{opt}_y}$ while increasing $\mathcal{E}_{\text{opt}_x}$ in the optimization problem (13). To balance these terms, we set $\lambda_W = 10^3$ for the remainder of the experiments.

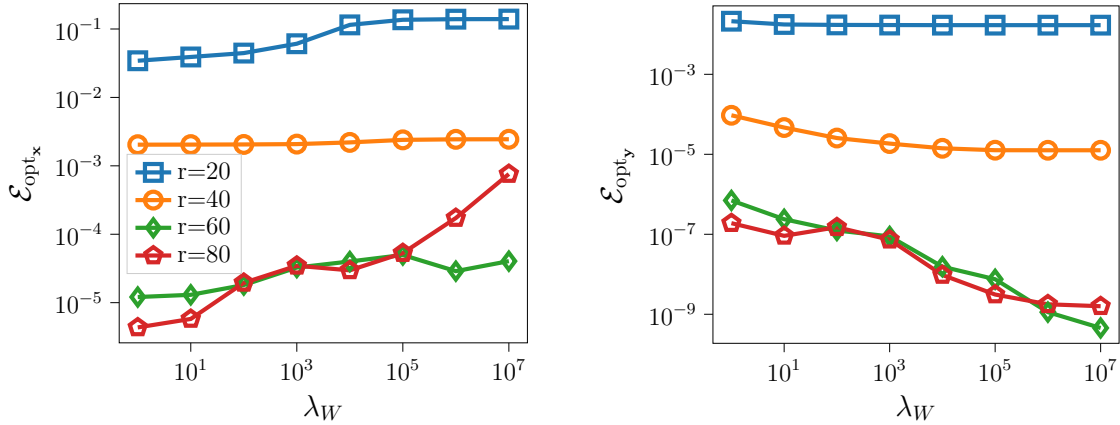


Figure 8: Toda Lattice Model: Optimization errors by pH-OpInf-W of r dimensions: $\mathcal{E}_{\text{opt}_x}$ (left) and $\mathcal{E}_{\text{opt}_y}$ (right).

Next, we examine the effect of the regularization parameter λ_R in the optimization problem (14)–(15), pH-OpInf-R. To this end, we pick eight values of λ_R from the set $\{10^{-14}, 10^{-13}, \dots, 10^{-7}\}$ for each value of r from $\{20, 40, 60, 80\}$. Figure 9 shows the corresponding optimization errors $\mathcal{E}_{\text{opt}_x}$ and $\mathcal{E}_{\text{opt}_y}$. For $r = 20$ and 40 , the errors remain relatively steady as λ_R varies. However, for the larger dimensions ($r = 60$ and 80), both optimization errors initially decrease and then increase after $\lambda_R = 10^{-11}$, consistent with the behavior observed in the linear case. Based on these observations, we set $\lambda_R = 10^{-11}$ in the subsequent experiments.

With $\lambda_W = 10^3$ in pH-OpInf-W and $\lambda_R = 10^{-11}$ in pH-OpInf-R, the minimum eigenvalues of the obtained \mathbf{R}_r are list in Table 2 for $r = 20, 40, 60$ and 80 , confirming the positive semi-definiteness of the inferred \mathbf{R}_r in both approaches.

Table 2: Toda Lattice Model: Minimum eigenvalues of \mathbf{R}_r obtained by pH-OpInf-W and pH-OpInf-R for different values of r .

	$r=20$	$r=40$	$r=60$	$r=80$
pH-OpInf-W	1.962×10^{-7}	3.857×10^{-6}	4.103×10^{-4}	4.074×10^{-4}
pH-OpInf-R	2.250×10^{-10}	2.924×10^{-6}	1.637×10^{-4}	1.168×10^{-4}

Test 2. Illustration of the error estimates

For this nonlinear pH system, we first consider pH-OpInf-ROM without using the hyper-reduction. To illustrate the error estimation given in Corollary 2.1, we choose a small time step size $\Delta t = 0.0025$ in both

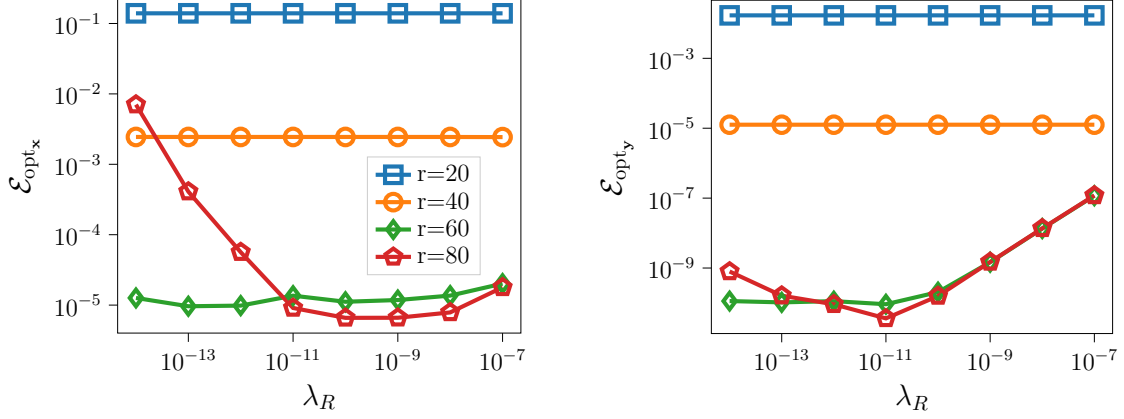


Figure 9: Toda Lattice Model: Optimization errors by pH-OpInf-R of r dimensions: $\mathcal{E}_{\text{opt}_x}$ (left) and $\mathcal{E}_{\text{opt}_y}$ (right).

FOM and ROM simulations, set $T_{\text{FOM}} = T_{\text{ROM}} = 50$ and vary the dimension r of the pH-OpInf-ROM from 10 to 100, increasing incrementally by 10. In this case, the singular values of the snapshot matrix \mathbf{X} decay more slowly than those in the mass-spring-damper case: the first 10 POD modes capture 97.97% of snapshot energy, the first 20 capture 99.8%, and the first 30 already capture 99.99%. The associated numerical errors defined in (31)–(36) are plotted in Figure 10: the left column corresponds to pH-OpInf-W, and the right column corresponds to pH-OpInf-R. Note that the magnitude of the state vectors is 2.225, while that of the output is 0.483. The top row displays \mathcal{E}_x , $\mathcal{E}_{\text{proj}_x}$ and $\mathcal{E}_{\text{opt}_x}$. For both pH-OpInf-W and pH-OpInf-R, $\mathcal{E}_{\text{opt}_x}$ decreases as the dimension r increases up to $r = 60$, beyond which it saturates. However, $\mathcal{E}_{\text{proj}_x}$ continues to decline until $r = 90$, for which it reaches machine precision. As a result, the state approximation error \mathcal{E}_x is dominated by $\mathcal{E}_{\text{opt}_x}$ and follows a similar trend. The output approximation error \mathcal{E}_y is shown alongside $\mathcal{E}_{\text{opt}_y}$ and \mathcal{E}_x in the middle row, from which we observe that the optimization error $\mathcal{E}_{\text{opt}_y}$ from pH-OpInf-R is smaller than that from pH-OpInf-W when r is bigger than 40. In both cases, $\mathcal{E}_{\text{opt}_y}$ is smaller than \mathcal{E}_x , thus the output approximation error \mathcal{E}_y is primarily influenced by \mathcal{E}_x and follows a similar pattern. The bottom row in Figure 10 compares the approximation errors of pH-OpInf-ROM with the intrusive SP-G-ROM. The results show that the pH-OpInf-ROM, based on either pH-OpInf-W or pH-OpInf-R, achieves better approximations than the intrusive SP-G-ROM for dimensions up to a fairly large dimension $r = 80$.

The time evolution of the output and approximate Hamiltonian from the pH-OpInf-ROMs is presented in Figure 11 when $r = 20, 40$ and 60 , respectively. We observe that the reduced-order approximations, using either pH-OpInf-W or pH-OpInf-R, get more accurate as r increases, and when $r = 40$, they closely align with those from the FOM simulation. Similar to the linear case in Section 5.2, although both achieve good approximations, the pH-OpInf-R attains a smaller optimization error $\mathcal{E}_{\text{opt}_y}$. Therefore, we use pH-OpInf-R in the subsequent experiments.

Test 3. Performance of hyper-reduction

Next, we apply hyper-reduction and test the performance of pH-OpInf-DEIM. The nonlinear Hamiltonian function in (38) is recast to

$$H(\mathbf{x}) = \frac{1}{2} \mathbf{x}^\top \mathbf{Q} \mathbf{x} + \mathbf{c}^\top h(\mathbf{x}), \quad \text{where} \quad \mathbf{Q} = \begin{bmatrix} \mathbf{0} & \mathbf{0} \\ \mathbf{0} & \mathbf{I}_{N_0} \end{bmatrix}_{n \times n}$$

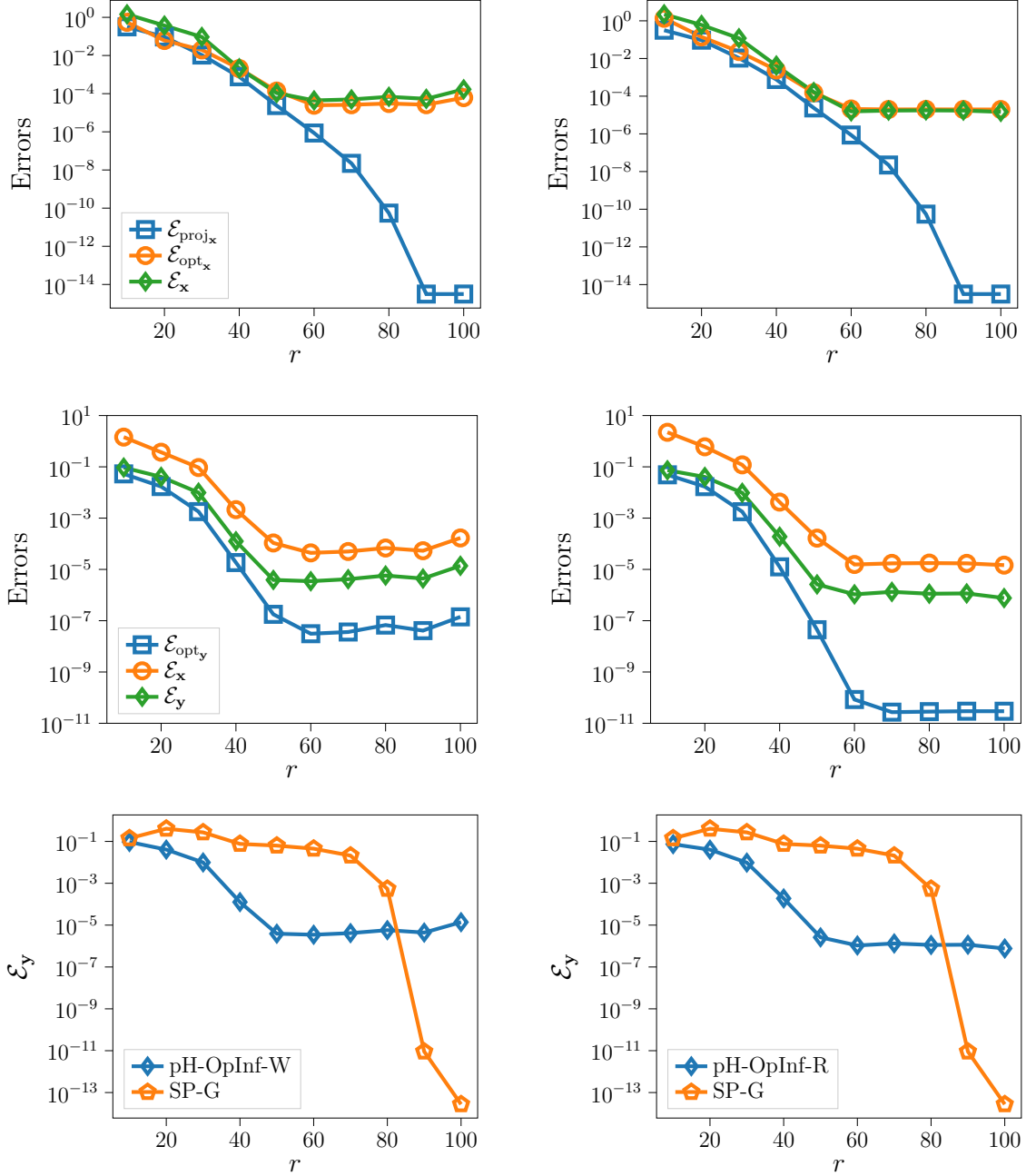


Figure 10: Toda Lattice Model: Numerical errors of pH-OpInf-W (left) and pH-OpInf-R (right) of r dimensions when $T_{\text{FOM}} = T_{\text{ROM}} = 50$.

and $\mathbf{c} = [1, 1, \dots, 1]^T \in \mathbb{R}^{N_0}$ with $h_1 = \exp(q_1 - q_2) - q_1 - N_0$, and $h_i = \exp(q_i - q_{i+1})$ for $i = 2, 3, \dots, N_0 - 1$ and $h_{N_0} = \exp(q_{N_0})$. Choosing $r = 20$ and 60 , respectively, we simulate the pH-OpInf-DEIM using m interpolation points in DEIM and compare it with the pH-OpInf-ROM of the same dimensions. The numerical errors in state and output approximations are listed in Table 3, together with the DEIM interpolation error $\mathcal{E}_{\text{DEIM}}$. Overall, $\mathcal{E}_{\text{DEIM}}$ decreases quickly as m increases. For both $r = 20$ and 60 , its precision reaches

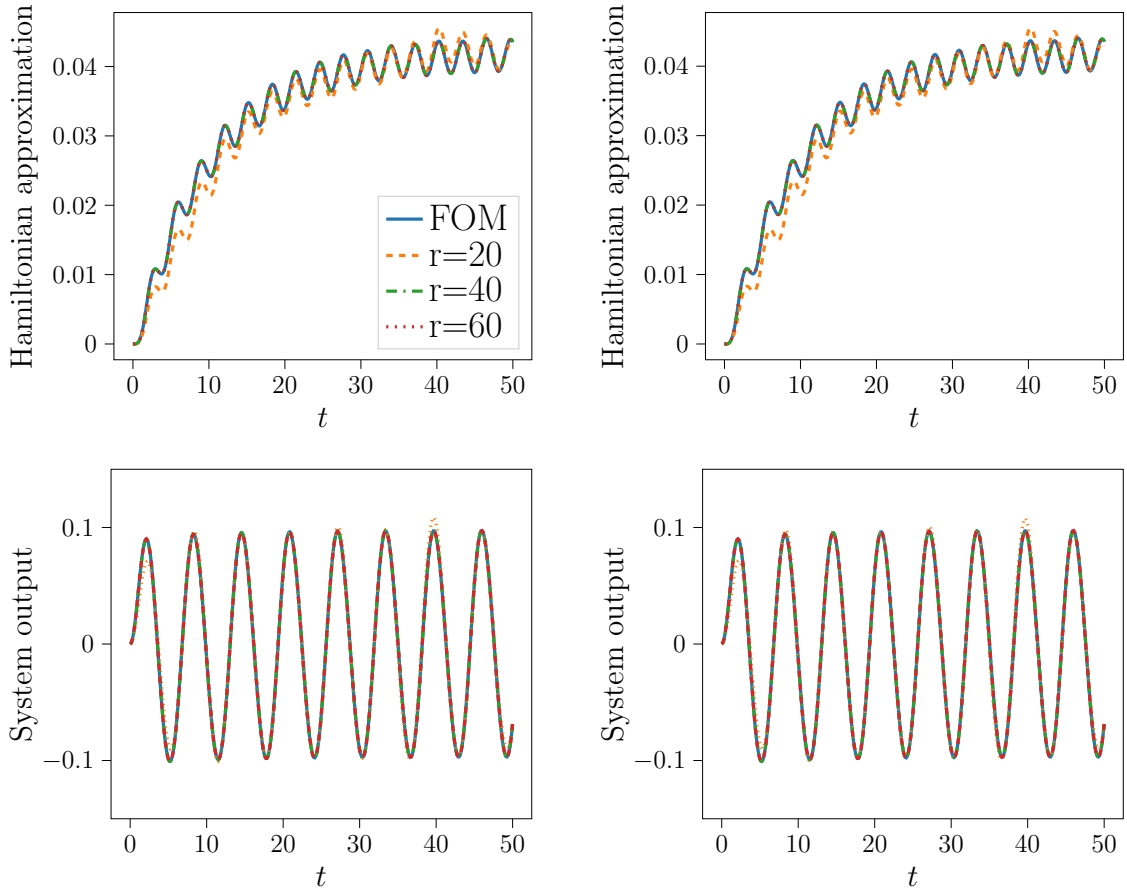


Figure 11: Toda Lattice Model: Hamiltonian approximation (top row) and system output (bottom row) from pH-OpInf-W (left) and pH-OpInf-R (right) of r dimensions, along with those of the FOM. All subplots share the same legend shown in the first one.

10^{-11} or higher when $m = 60$, and the pH-OpInf-DEIM results coincide with those of pH-OpInf-ROM. This observation matches our theoretical results, as stated in Theorems 1 and 2, because, comparing with pH-OpInf-ROM, the error bound of pH-OpInf-DEIM involves the additional term $\mathcal{E}_{\text{DEIM}}$. When $\mathcal{E}_{\text{DEIM}}$ is sufficiently small, errors from both ROMs should become identical.

Test 4. Performance at a different input

We test pH-OpInf-ROM and pH-OpInf-DEIM using an input that differs from the training input. Particularly, to infer the reduced operators, we use the training input $u(t) = 0.1 \sin(t)$, as shown in Figure 12 (left), and simulate the reduced-order systems with a testing input, as shown in Figure 12 (right). The sawtooth signal is discontinuous, which makes the test challenging. Figure 13 compares the system output and the Hamiltonian function obtained by simulating the pH-OpInf-ROM with dimension $r = 50$ and the pH-OpInf-DEIM with the same dimension and $m = 50$, along with the FOM results. Both pH-OpInf-ROM and pH-OpInf-DEIM are able to accurately capture the system output in response to the testing input and effectively approximate the Hamiltonian function during the simulation.

	pH-OpInf-ROM with $r = 20$	pH-OpInf-DEIM with $r = 20$			
		$m = 30$	$m = 40$	$m = 50$	$m = 60$
\mathcal{E}_x	6.042×10^{-1}	6.494×10^{-1}	5.958×10^{-1}	6.042×10^{-1}	6.042×10^{-1}
\mathcal{E}_y	4.032×10^{-2}	4.400×10^{-2}	4.030×10^{-2}	4.032×10^{-2}	4.032×10^{-2}
$\mathcal{E}_{\text{DEIM}}$	-	3.985×10^{-2}	7.552×10^{-4}	4.095×10^{-8}	4.585×10^{-15}

	pH-OpInf-ROM with $r = 60$	pH-OpInf-DEIM with $r = 60$			
		$m = 50$	$m = 55$	$m = 60$	$m = 65$
\mathcal{E}_x	1.719×10^{-4}	1.745×10^{-4}	1.719×10^{-4}	1.719×10^{-4}	1.719×10^{-4}
\mathcal{E}_y	7.748×10^{-6}	7.781×10^{-6}	7.748×10^{-6}	7.748×10^{-6}	7.748×10^{-6}
$\mathcal{E}_{\text{DEIM}}$	-	1.184×10^{-5}	4.384×10^{-9}	3.478×10^{-11}	1.737×10^{-13}

Table 3: Toda Lattice Model: Errors of pH-OpInf-ROM with dimension r and pH-OpInf-DEIM with the same dimension using m DEIM interpolation points.

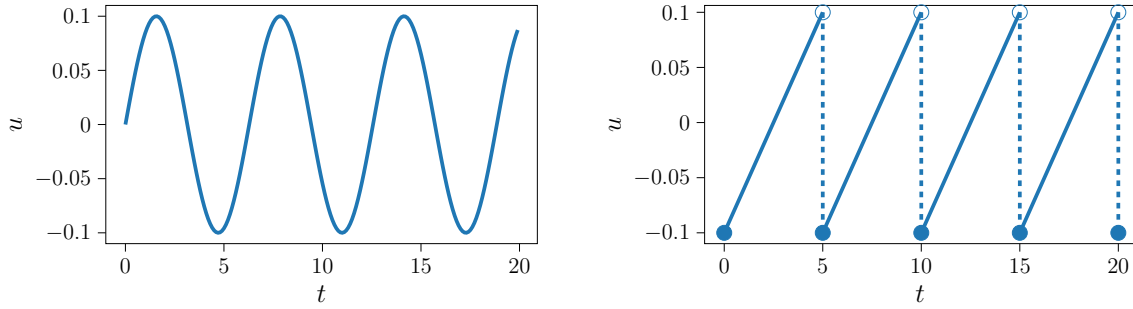


Figure 12: Toda Lattice Model: Training input (left) and testing input (right) for Test 4.

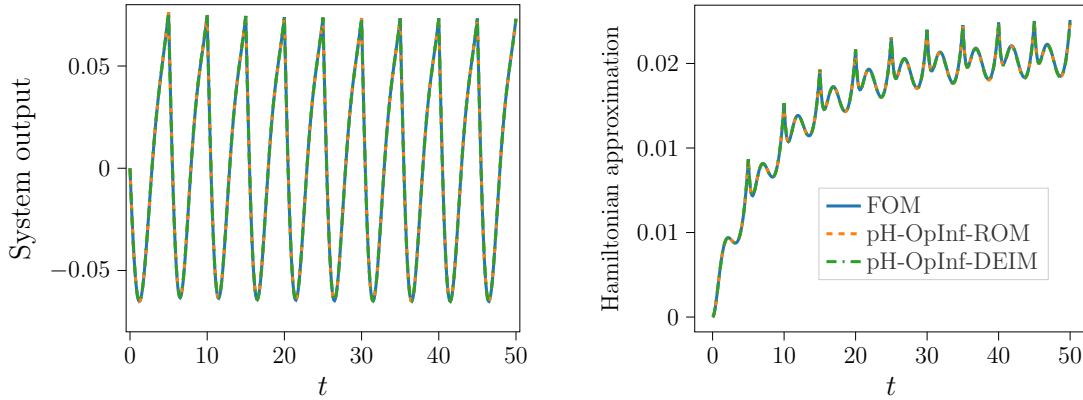


Figure 13: Toda Lattice Model: Simulation results of pH-OpInf-ROM for $r = 50$, pH-OpInf-DEIM for $r = 50$ and $m = 50$, and the FOM: system output (left) and Hamiltonian approximation (right) for Test 4.

6. Conclusions

In this work, we have extended the operator inference framework to learn structure-preserving reduced-order models for port-Hamiltonian systems. By leveraging data of the system's state, input, and output, as well as the Hamiltonian function, we formulate two optimization problems and corresponding ROMs,

pH-OpInf-W and pH-OpInf-R, for inferring reduced-order operators that retain the physical properties and geometric structure of the original system. The former finds reduced operators, \mathbf{B}_r and \mathbf{D}_r (hence \mathbf{J}_r and \mathbf{R}_r), simultaneously by solving a semi-definite optimization, while the latter decouples the optimization into two steps: the first step determines the reduced operator \mathbf{B}_r using regularized least squares, and the second step identifies the other reduced operator \mathbf{D}_r through a semi-definite optimization. Based on the reduced-order operators, the low-dimensional pH-OpInf-ROM can be constructed. To further address the challenges of evaluating nonlinear terms in the ROM, we use a DEIM-based hyper-reduction method, which leads to the pH-OpInf-DEIM model. We analyze the corresponding approximation errors in the system's state and output and numerically verify them through experiments on a linear mass-spring-damper system and a nonlinear Toda lattice model.

The numerical results show that both pH-OpInf-W and pH-OpInf-R with carefully chosen optimization parameters find reduced-order operators that preserve the appropriate structures. Generally, the overall performance of these two approaches is comparable, since the pH-OpInf-ROM constructed using either approach yields accurate outputs in response to inputs. However, pH-OpInf-R achieves a smaller optimization error for the output, $\mathcal{E}_{\text{opt}_y}$, than pH-OpInf-W, which makes it the preferred choice. Furthermore, for nonlinear pH systems, the pH-OpInf-DEIM model using sufficient DEIM interpolation points is able to achieve the same performance at a reduced computational cost. We note that alternative hyper-reduction approaches, such as ECSW [52], may also be applied to inferred ROMs when they are nonlinear. We will investigate their performance in future work.

Acknowledgement

Y.G. was partially supported by the SPARC grant from the University of South Carolina under award number CL071-130600-N1400-202-80006259-1. L.J. was partially supported by the U.S. Department of Energy under award numbers DE-SC0022254 and DE-SC0025527. B.K. and Z.W. were supported by U.S. Office of Naval Research under award number N00014-22-1-2624. Z.W. was partially supported by U.S. National Science Foundation under award numbers DMS-2012469, DMS-2038080, DMS-2245097 and an ASPIRE grant from the Office of the Vice President for Research at the University of South Carolina.

References

- [1] A. Van Der Schaft, D. Jeltsema, et al., Port-Hamiltonian systems theory: An introductory overview, *Foundations and Trends® in Systems and Control* 1 (2-3) (2014) 173–378.
- [2] V. Duindam, A. Macchelli, S. Stramigioli, H. Bruyninckx, *Modeling and control of complex physical systems: the port-Hamiltonian approach*, Springer Science & Business Media, 2009.
- [3] E. Hairer, M. Hochbruck, A. Iserles, C. Lubich, *Geometric numerical integration*, *Oberwolfach Reports* 3 (1) (2006) 805–882.
- [4] A. Quarteroni, A. Manzoni, F. Negri, *Reduced basis methods for partial differential equations: an introduction*, Vol. 92, Springer, 2015.
- [5] P. Holmes, *Turbulence, coherent structures, dynamical systems and symmetry*, Cambridge university press, 2012.
- [6] J. N. Kutz, S. L. Brunton, B. W. Brunton, J. L. Proctor, *Dynamic mode decomposition: data-driven modeling of complex systems*, SIAM, 2016.

- [7] P. J. Schmid, Dynamic mode decomposition and its variants, *Annual Review of Fluid Mechanics* 54 (1) (2022) 225–254.
- [8] B. Kramer, B. Peherstorfer, K. E. Willcox, Learning nonlinear reduced models from data with operator inference, *Annual Review of Fluid Mechanics* 56 (2024) 521–548.
- [9] B. Peherstorfer, K. Willcox, Data-driven operator inference for nonintrusive projection-based model reduction, *Computer Methods in Applied Mechanics and Engineering* 306 (2016) 196–215.
- [10] A. C. Antoulas, *Approximation of large-scale dynamical systems*, SIAM, 2005.
- [11] A. C. Antoulas, C. A. Beattie, S. Güğercin, *Interpolatory methods for model reduction*, SIAM, 2020.
- [12] P. Benner, S. Gugercin, K. Willcox, A survey of projection-based model reduction methods for parametric dynamical systems, *SIAM review* 57 (4) (2015) 483–531.
- [13] J. S. Hesthaven, G. Rozza, B. Stamm, et al., *Certified reduced basis methods for parametrized partial differential equations*, Vol. 590, Springer, 2016.
- [14] S. Lall, P. Krysl, J. E. Marsden, Structure-preserving model reduction for mechanical systems, *Physica D: Nonlinear Phenomena* 184 (1-4) (2003) 304–318.
- [15] K. Carlberg, R. Tuminaro, P. Boggs, Preserving Lagrangian structure in nonlinear model reduction with application to structural dynamics, *SIAM Journal on Scientific Computing* 37 (2) (2015) B153–B184.
- [16] Y. Gong, Q. Wang, Z. Wang, Structure-preserving Galerkin POD reduced-order modeling of Hamiltonian systems, *Computer Methods in Applied Mechanics and Engineering* 315 (2017) 780–798.
- [17] Y. Miyatake, Structure-preserving model reduction for dynamical systems with a first integral, *Japan Journal of Industrial and Applied Mathematics* 36 (3) (2019) 1021–1037.
- [18] R. Barbulescu, G. Ciuprina, T. Ionescu, D. Ioan, L. M. Silveira, Efficient model reduction of myelinated compartments as port-Hamiltonian systems, in: *Scientific Computing in Electrical Engineering: SCEE 2020*, Eindhoven, The Netherlands, February 2020, Springer, 2021, pp. 3–12.
- [19] C. Beattie, S. Gugercin, Structure-preserving model reduction for nonlinear port-Hamiltonian systems, in: *2011 50th IEEE conference on decision and control and European control conference*, IEEE, 2011, pp. 6564–6569.
- [20] S. Chaturantabut, C. Beattie, S. Gugercin, Structure-preserving model reduction for nonlinear port-Hamiltonian systems, *SIAM Journal on Scientific Computing* 38 (5) (2016) B837–B865.
- [21] L. Peng, K. Mohseni, Symplectic model reduction of Hamiltonian systems, *SIAM Journal on Scientific Computing* 38 (1) (2016) A1–A27.
- [22] A. Gruber, I. Tezaur, Variationally consistent Hamiltonian model reduction, *SIAM Journal on Applied Dynamical Systems* 24 (1) (2025) 376–414.
- [23] B. M. Afkham, J. S. Hesthaven, Structure preserving model reduction of parametric Hamiltonian systems, *SIAM Journal on Scientific Computing* 39 (6) (2017) A2616–A2644.

- [24] J. Hesthaven, C. Pagliantini, Structure-preserving reduced basis methods for Poisson systems, *Mathematics of Computation* 90 (330) (2021) 1701–1740.
- [25] C. Pagliantini, Dynamical reduced basis methods for Hamiltonian systems, *Numerische Mathematik* 148 (2) (2021) 409–448.
- [26] J. S. Hesthaven, C. Pagliantini, G. Rozza, Reduced basis methods for time-dependent problems, *Acta Numerica* 31 (2022) 265–345.
- [27] M. Barrault, Y. Maday, N. C. Nguyen, A. T. Patera, An ‘empirical interpolation’ method: application to efficient reduced-basis discretization of partial differential equations, *Comptes Rendus Mathematique* 339 (9) (2004) 667–672.
- [28] S. Chaturantabut, D. C. Sorensen, Nonlinear model reduction via discrete empirical interpolation, *SIAM Journal on Scientific Computing* 32 (5) (2010) 2737–2764.
- [29] C. Pagliantini, F. Vismara, Gradient-preserving hyper-reduction of nonlinear dynamical systems via discrete empirical interpolation, *SIAM Journal on Scientific Computing* 45 (5) (2023) A2725–A2754.
- [30] H. Sharma, H. Mu, P. Buchfink, R. Geelen, S. Glas, B. Kramer, Symplectic model reduction of Hamiltonian systems using data-driven quadratic manifolds, *Computer Methods in Applied Mechanics and Engineering* 417 (2023) 116402.
- [31] S. Yıldız, P. Goyal, T. Bendokat, P. Benner, Data-driven identification of quadratic representations for nonlinear Hamiltonian systems using weakly symplectic liftings, *Journal of Machine Learning for Modeling and Computing* 5 (2).
- [32] P. Buchfink, S. Glas, B. Haasdonk, Symplectic model reduction of Hamiltonian systems on nonlinear manifolds and approximation with weakly symplectic autoencoder, *SIAM Journal on Scientific Computing* 45 (2) (2023) A289–A311.
- [33] H. Sharma, Z. Wang, B. Kramer, Hamiltonian operator inference: Physics-preserving learning of reduced-order models for canonical Hamiltonian systems, *Physica D: Nonlinear Phenomena* 431 (2022) 133122.
- [34] A. Gruber, I. Tezaur, Canonical and noncanonical Hamiltonian operator inference, *Computer Methods in Applied Mechanics and Engineering* 416 (2023) 116334.
- [35] Y. Geng, J. Singh, L. Ju, B. Kramer, Z. Wang, Gradient preserving operator inference: Data-driven reduced-order models for equations with gradient structure, *Computer Methods in Applied Mechanics and Engineering* 427 (2024) 117033.
- [36] A. Vijaywargiya, S. A. McQuarrie, A. Gruber, Tensor parametric Hamiltonian operator inference, *arXiv preprint arXiv:2502.10888*.
- [37] K. Cherifi, P. K. Goyal, P. Benner, A non-intrusive method to inferring linear port-Hamiltonian realizations using time-domain data, *Electronic Transactions on Numerical Analysis: Special Issue SciML* 56 (2022) 102–116.
- [38] R. Morandin, J. Nicodemus, B. Unger, Port-Hamiltonian dynamic mode decomposition, *SIAM Journal on Scientific Computing* 45 (4) (2023) A1690–A1710.

- [39] G. Berkooz, P. Holmes, J. L. Lumley, The proper orthogonal decomposition in the analysis of turbulent flows, *Annual review of fluid mechanics* 25 (1) (1993) 539–575.
- [40] S. Gugercin, R. V. Polyuga, C. Beattie, A. Van Der Schaft, Structure-preserving tangential interpolation for model reduction of port-Hamiltonian systems, *Automatica* 48 (9) (2012) 1963–1974.
- [41] Z. Drmac, S. Gugercin, A new selection operator for the discrete empirical interpolation method—improved a priori error bound and extensions, *SIAM Journal on Scientific Computing* 38 (2) (2016) A631–A648.
- [42] C. Helmberg, F. Rendl, R. J. Vanderbei, H. Wolkowicz, An interior-point method for semidefinite programming, *SIAM Journal on optimization* 6 (2) (1996) 342–361.
- [43] S. Chaturantabut, D. C. Sorensen, A state space error estimate for POD-DEIM nonlinear model reduction, *SIAM Journal on numerical analysis* 50 (1) (2012) 46–63.
- [44] G. Dahlquist, Stability and error bounds in the numerical integration of ordinary differential equations, Ph.D. thesis, Almqvist & Wiksell (1958).
- [45] K. Kunisch, S. Volkwein, Galerkin proper orthogonal decomposition methods for parabolic problems, *Numerische mathematik* 90 (2001) 117–148.
- [46] J. R. Singler, New POD error expressions, error bounds, and asymptotic results for reduced order models of parabolic PDEs, *SIAM Journal on Numerical Analysis* 52 (2) (2014) 852–876.
- [47] B. Peherstorfer, Sampling low-dimensional Markovian dynamics for preasymptotically recovering reduced models from data with operator inference, *SIAM Journal on Scientific Computing* 42 (5) (2020) A3489–A3515.
- [48] R. V. Polyuga, Model reduction of port-Hamiltonian systems.
- [49] M. ApS, Mosek optimization toolbox for matlab, User’s Guide and Reference Manual, Version 4 (1).
- [50] S. Diamond, S. Boyd, Cvxpy: A python-embedded modeling language for convex optimization, *Journal of Machine Learning Research* 17 (83) (2016) 1–5.
- [51] A. Agrawal, R. Verschueren, S. Diamond, S. Boyd, A rewriting system for convex optimization problems, *Journal of Control and Decision* 5 (1) (2018) 42–60.
- [52] C. Farhat, T. Chapman, P. Avery, Structure-preserving, stability, and accuracy properties of the energy-conserving sampling and weighting method for the hyper reduction of nonlinear finite element dynamic models, *International journal for numerical methods in engineering* 102 (5) (2015) 1077–1110.